Control Engineering Practice 90 (2019) 1–18

Contents lists available at ScienceDirect

Control Engineering Practice

journal homepage: www.elsevier.com/locate/conengprac

Optimized techniques for driving and control of the switched reluctance motor to improve efficiency

Marcio Rodrigues da Cunha Reis [a,b,c,d,*], Wanderson Rainer Hilario de Araujo [b,d], Viviane Margarida Gomes [a,b,c], Felippe dos Santos e Silva [a], Cleber Asmar Ganzaroli [a,b], Flavio Adalberto Gomes [a,b], Gabriel Andres Wainer [c], Wesley Pacheco Calixto [a,b,c,*]

[a] Studies and Researches in Science and Technology Group (GCITE), Federal Institute of Goias (IFG), 75250-000, Senador Canedo, Goias, Brazil
[b] Electrical, Mechanical & Computer Engineering School (EMC), Federal University of Goias (UFG), Goiania, Goias, Brazil
[c] Visualization, Simulation and Modeling (VSIM), Carleton University, Ottawa, Canada
[d] Engineering School, Pontifical Catholic University of Goias (PUC-GO), Goiania, Goias

ARTICLE INFO

Keywords:
Switched reluctance motor
Simulation
Identification and modeling systems
Optimized techniques
Driving and control
Classical control
Improve efficiency

ABSTRACT

This work presents modeling, driving and classical speed control techniques for the switched reluctance motor. The aim is to improve the computational model, the control response and the machine efficiency. A parametric regression model was used to find the inductance profile of the switched reluctance motor and from the new inductance profile model. The drive and control techniques are shown: (i) with speed control acting on the excitation voltage and fixed switching angles, (ii) with speed control acting on the switching angles and fixed excitation voltage and (iii) with speed control acting on the excitation voltage, in this case, with dynamic switching angles and controller parameters. The inductance profile is represented by expression and inserted into the machine computer model, allowing greater precision and low computational cost. The speed control acting on the excitation voltage with dynamic controller parameters and dynamic switching angles allowed: (i) shorter response time for a wide range of control, (ii) higher efficiency, (iii) low computational cost and (iv) simplified implementation and maintenance. The techniques proposed in this work obtained precision of the computational model with respect to the system (in workbench) and optimized parameters in a wide range of the speed control, allowing an improvement of switched reluctance motor efficiency.

1. Introduction

Studies related to the switched reluctance machine have increased due to the favorable features of this device. Characteristics such as: (i) relatively simple manufacturing, (ii) low manufacturing cost, (iii) high power density, (iv) use as a motor and generator, (v) low speed and high speed operation and others (Kazmierkowski, Blaabjerg, & Krishnan, 2002). Like all electric machines, the switched reluctance machine enables the reversibility of the energy conversion, and can operate as an engine or as a generator (Fitzgerald, Kingsley, & Umans, 2013; Kosow, 1991). The machine has been in several researches related to the operation as motor and as generator (Araujo, 2006; Silveira et al., 2009). The switched reluctance machine is attractive for industrial applications that require, above all, wide speed range and high torque values (Rashid, 2014). Even with several studies regarding this device, there is still a need to increase efficiency by giving reliability to the system and ensure the reduction of electric energy consumption. In addition, is necessary the development of greater performance controllers and simplified implementation and maintenance (Araujo, 2006; Ogata, 2009; Rashid, 2014).

The switched reluctance motor (SRM) arouses the interest of the automotive and aerospace industries by being able to operate as a starter motor-generator (Shaoping & Qingfu, 2001). A study with experimental data is presented for automotive starter motor in Silveira et al. (2009), which aims to perform the control of changing the operating mode of the machine (motor or generator) for better efficiency. The used technique is based on acting at the coil switching instants using microprocessed systems. The machine operates as a motor at starting the car and when the engine is running the machine operates as a generator supplying the power demand of the vehicle's electrical and electronic components.

Due to demands for sustainable development, numerous researches are focused on the design of electric cars and hybrids, avoiding the use of fossil fuels. The Aida & Miki studies (Watanabe, Aida, Komatsuzaki, & Miki, 2008) present the modeling of the adaptation between combustion vehicle and electric vehicle using three-phase SRM with 12 poles topology in the stator and 8 poles in the rotor (12 × 8). In the same way another study presents the electric vehicle construction where

* Corresponding authors.
E-mail addresses: marcio.reis@ifg.edu.br, marciorcreis@gmail.com (M.R. da Cunha Reis), wpcalixto@pq.cnpq.br (W.P. Calixto).

https://doi.org/10.1016/j.conengprac.2019.06.007
Received 4 June 2018; Received in revised form 11 June 2019; Accepted 13 June 2019
Available online 19 June 2019
0967-0661/

the SRM is coupled directly to the traction axis (Fujishiro, Ishikawa, Kikuchi, Nakamura, & Ichinokura, 2006). In this case, an alternative SRM topology was used, with the stator properly wound on the inside of the machine and the solid rotor rotating around the stator.

In most studies related to the SRM it is necessary to employ computational simulations that aid in the development of projects and researches. The computational models presented by the scientific community are diversified (Viajante et al., 2013). Such models generally depend directly on how the machine inductances are represented, directly impacting the computational model response (Law & Kelton, 2000).

Andrade and Krishnan (2001) present nonlinear analytical method for the representation of the machine phase inductance. The method is based on the Fourier series with adjustable coefficients. To evaluate the accuracy of the proposal, the authors compare the simulation results with a model that uses the finite element method (FEM). According to Andrade and Krishnan (2001), the technique is able to characterize the inductance profile of the switched reluctance machine.

Araujo (2006) presents design, simulation, construction and drive for the switched reluctance motor. Studies are carried out on switching systems and a proposal for an alternative technique. The technique proposed by Araujo (2006) allows the control through the instantaneous current, realized by microprocessed system, providing action of control of two states on the switched of the power converter. In that work the author implements and compares the drive systems, stating that the proposed drive technique reduces the losses by switching.

The implementation of electromechanical systems requires the increasing demand for control techniques, more specifically automatic control. Proportional, integral and derivative control (PID) is a classic tool with low computational effort (Ogata, 2009). The work of Su, Zhang, Wang, and Dai (2017) develops control of the switched reluctance motor. The PID control and the dynamic PID control are developed for the SRM, where the authors perform simulation test and present the effectiveness of the dynamic PID controller that can achieve better response time and lower overshoot when compared to the classic PID controller, even when subject to disturbances (Su et al., 2017).

The chronological order of the works cited is presented in Table 1.

Several studies have used the most varied models of inductance profile, different types of controllers and heuristic optimization methods applied to the SRM. However, there is still a gap where the switched reluctance motor operates with optimized control over a wide speed range under varying mechanical load and the use of drive technology that provides greater energy efficiency in the control conditions. According to work already done, it is necessary to improve the technique of mapping the inductance profile of the SRM considering the magnetic saturation, considering the reliability of simulation results and reduction of the computational effort, thus justifying this work.

This work proposes a representation model for the windings inductance of the switched reluctance motor in order to approximate the computational model to the experimental one (Araujo et al., 2017; Gomes et al., 2017). Operational techniques are also proposed together with a speed controller to improve control performance and machine efficiency. This work presents in Section 2 the mathematical modeling of the SRM, the inductance and simulation profile. The proposed methodology for driving and control of the SRM is described in Sections 3 and 4 shows the results.

2. Mathematical model of the switched reluctance motor

The conventional SRM drive requires constant information of instantaneous rotor position for the correct energization of its phases. The advance in electronics and microprocessed systems have boosted in recent years the research and innovation related to the SRM (Viajante et al., 2013). Switched reluctance machines are generally composed of steel blade packs and the number of stator and rotor poles can take various configurations (Andrade & Krishnan, 2001). Fig. 1(a) shows the cross-section of a 6 × 4 SRM highlighting the one-phase coil (Araujo, 2006). The application of current in the SRM coils is performed through the half-bridge (Kazmierkowski et al., 2002; Rashid, 2014; Viajante et al., 2013) power converter, which is illustrated in Fig. 1(b).

In the circuit shown in Fig. 1(b), Q are electronic switches that are driven by microprocessed system obeying the increasing inductance region to produce positive torque (Araujo, 2006; Hannoun, Hilairet, & Marchand, 2011). The instant information of the rotor position is usually obtained by optical sensors or encoders connected to the machine shaft. The inductor L refers to the inductive characteristic per phase, D are diodes capable of conducting the electric current stored in the coil when the switches Q are turned off and c the amount of phases that the SRM possesses. The amount of phases c defines the amount of keys Q and diodes D that will be added to the half-bridge converter. The RL circuit formed by the coil shown in Fig. 1 is associated to the magnetic circuit provided by the core, which can be analyzed by:

$$V = R \cdot i + \frac{d\lambda(t)}{dt} = R \cdot i + L \cdot \frac{di(t)}{dt} + e \tag{1}$$

where V is the voltage applied at the coil terminals in volts [V], R is the coil resistance in ohms [Ω], i is the current in the coil in amperes [A], L is the inductance of the coil in henry [H], and t the time in seconds [s]. The force counter electromotive force is given by Kosow (1991):

$$e = \omega \cdot i \cdot \frac{\partial L(\theta, i)}{\partial \theta} \tag{2}$$

where ω is the rotor angular speed in radians per second [rad/s], described as $\omega = \frac{d\theta}{dt}$, and θ is position angle of the rotor in degrees [°]. Regarding the electromechanical expressions, the torque developed by the motor T_m and the efficiency η are defined by:

$$T_{mag} = T_m + D \cdot \omega + J \cdot \frac{d\omega(t)}{dt} \tag{3}$$

$$\eta = \frac{P_m}{P_e} = \frac{T_m \cdot \omega}{V_{exc} \cdot I_{exc}} \tag{4}$$

where T_m is given in newton meter [N m], η is the relationship between the mechanical power produced P_m and the electric power consumed P_e, T_{mag} is the electromagnetic torque in [N m], D is the coefficient of friction in [(N s)/rad], J is the inertia [(N ms^2)/rad], V_{exc} is the DC excitation voltage in [V] and I_{exc} is the excitation current of the DC bus in [A]. The object of this study is a motor that has 6 poles in the stator and 4 poles in the rotor (configuration 6 × 4). Thus, considering the contribution of the three phases and the mechanical equation, the mathematical model of the SRM can be represented by the state equation, given by Kazmierkowski et al. (2002), N.d.S. (2010) and Zheng, Zhao, and Wei (2009):

$$V_{(5\times1)} = R_{(5\times5)} \cdot I_{(5\times1)} + L_{(5\times5)} \cdot \dot{I}_{(5\times1)} \tag{5}$$

where the state matrices are given by:

$$V = \begin{bmatrix} V_a \\ V_b \\ V_c \\ T_m \\ 0 \end{bmatrix} \text{ and } R = \begin{bmatrix} R_a & 0 & 0 & 0 & 0 \\ 0 & R_b & 0 & 0 & 0 \\ 0 & 0 & R_c & 0 & 0 \\ r_1 & r_2 & r_3 & D & 0 \\ 0 & 0 & 0 & -1 & 0 \end{bmatrix} \tag{6}$$

$$L = \begin{bmatrix} L_a & 0 & 0 & 0 & i_a \frac{\partial L_a(\theta, i)}{\partial \theta} \\ 0 & L_b & 0 & 0 & i_b \frac{\partial L_b(\theta, i)}{\partial \theta} \\ 0 & 0 & L_c & 0 & i_c \frac{\partial L_c(\theta, i)}{\partial \theta} \\ 0 & 0 & 0 & J & 0 \\ 0 & 0 & 0 & 0 & 1 \end{bmatrix} \text{ and } \dot{I} = \begin{bmatrix} \dot{i}_a \\ \dot{i}_b \\ \dot{i}_c \\ \dot{\omega} \\ \dot{\theta} \end{bmatrix} \tag{7}$$

Table 1
Order of project development, modeling, drive and control using switched reluctance motors.

Approach	Reference	Description
Modeling and Simulation	Silveira et al. (2009)	Study with automotive starter motor with SRM
Modeling and Drive	Watanabe et al. (2008)	Present the modeling of adaptation between combustion vehicle and electric vehicle using SRM
Design and construction	Fujishiro et al. (2006)	Present the electric vehicle construction with SRM
Nonlinear based modeling	Andrade and Krishnan (2001)	Present a nonlinear analytical method for SRM phase inductance
Design, construction and drive	Araujo (2006)	Presents design, simulation, construction and drive for the SRM
Modern drive and control	Su et al. (2017)	Develops static and dynamic control for SRM

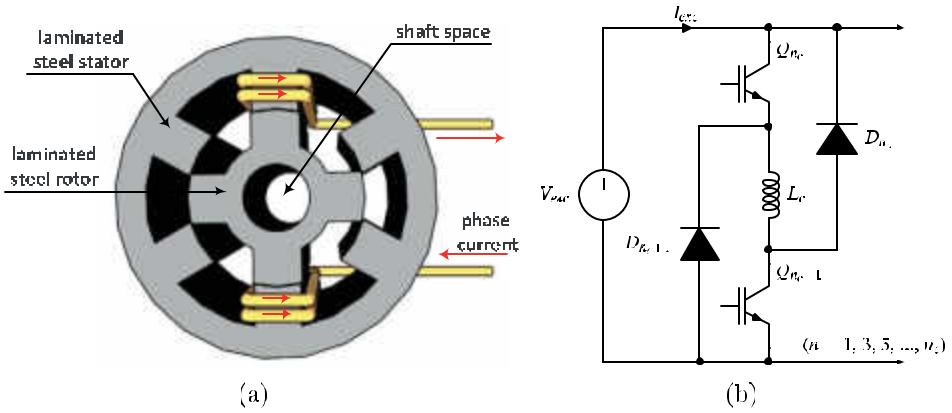

Fig. 1. Drive representation of a SRM phase: (a) cross-section of a single-phase switched reluctance machine and (b) half-bridge power converter.

In (6) and (7), V_a, V_b, V_c, R_a, R_b and R_c are respectively the applied voltages and the resistances of the coils referring to the 3 phase SRM 6 × 4 and $\dot{I}$ is the first derivate of I. The terms r_1, r_2 and r_3 are given by Araujo (2006):

$$r_1 = \frac{1}{2}\cdot i_a \cdot \frac{\partial L_a(\theta,i)}{\partial\theta},\quad r_2 = \frac{1}{2}\cdot i_b \cdot \frac{\partial L_b(\theta,i)}{\partial\theta} \text{ and } r_3 = \frac{1}{2}\cdot i_b \cdot \frac{\partial L_c(\theta,i)}{\partial\theta} \quad (8)$$

With (5), (6), (7) and (8) it is possible to obtain the model that represents each phase of the machine. Thus, when voltage is applied under conditions that the inductance promotes positive torque (machine operating as motor), the current calculated using this model will be given by:

$$\dot{I}_{(5\times1)} = L^{-1}_{(5\times5)} \cdot V_{(5\times1)} - L^{-1}_{(5\times5)} \cdot R_{(5\times5)} \cdot I_{(5\times1)} \quad (9)$$

The matrix elements R and L are parameters that depend on the constructive aspects of the machine. The values of resistances of the coils are parameters with relative simplicity of experimental obtaining. However, the inductance of the coil depends on the angular position of the rotor θ and the applied current i. Therefore, it is possible to conclude that such parameters, mainly the inductances and their derivatives, are extremely important for SRM mathematical model (Andrade & Krishnan, 2001; Araujo et al., 2017).

2.1. Inductance profile models

There are several studies related to the computational models for SRM (Hannoun et al., 2011; Kazmierkowski et al., 2002; Viajante et al., 2013). Each model has its specificity and perform calculations of variables and their variations according to the expression (9). Thus, the greatest divergences between the models are concentrated in the way the inductance of SRM windings and their derivatives are represented, which impacts the behavior of electrical and mechanical magnitudes of the machine during the simulation (Araujo et al., 2017). Fig. 2 illustrates the block diagram of the simulation for SRM considering the mathematical model in (9).

In Fig. 2, g_1, g_2, and g_3 represent the trigger signals for each phase of the half-bridge converter and the **inductance profile** block, shown on the right in Fig. 2, represents the inductance profile of the SRM windings and their respective derivatives. The computational simulation of the SRM seeks to relate the energy converter circuit to the mathematical model and the inductance profile representation directly affects the accuracy of the simulation when compared to the experimental model (Araujo, 2006). Among the inductance profile models, the simplest model is linear because it does not consider the magnetic saturation of the machine core. In this model, it is assumed that the inductances have sinusoidal behavior as a function of the angular position of the rotor and is given by:

$$L(\theta) = \frac{L_{\max} + L_{\min}}{2} + \frac{L_{\max} - L_{\min}}{2}\cdot\cos(4\cdot\theta + \zeta) \quad (10)$$

where ζ is the angle per phase, in which phase A $\zeta_a = 0°$, phase B $\zeta_b = -60°$, phase C $\zeta_c = +60°$, $L_{\max}$ and $L_{\min}$ are respectively the maximum and minimum inductance of the SRM windings.

In the case of the linear model, state change rates are easily obtained. Although the linear model provides an indication of the SRM operation principle as a motor, as well as the dynamic behavior of some quantities, it does not obtain answers with desired precision when the results obtained by the model are compared to the results obtained experimentally (Araujo et al., 2017).

Nonlinear inductance profile models and their derivatives consider the saturation of the magnetic material. When using non-linear models, inductance points (or concatenated flux) must be calculated as a function of the rotor angular position for each current value, thus obtaining the inductance surface (Andrade & Krishnan, 2001; Silveira et al., 2009; Viajante et al., 2013). These points are found experimentally or through the finite element method (FEM) (Araujo, 2006). One of the nonlinear inductance profile models employed in several studies is the Fourier series approximation. This model considers that since the coil inductance is periodic (Kazmierkowski et al., 2002), the inductance values in several segments of lines are discretized to compose the inductive behavior (Andrade & Krishnan, 2001; Viajante et al., 2013).

In the model of Fourier series approximation, the positions where the inductance has maximum and minimum values do not have the same behavior, as in the case of the linear model, where the inductance is sinusoidal (Araujo, 2006). Another nonlinear inductance profile model, which is an alternative to the Fourier series approximation

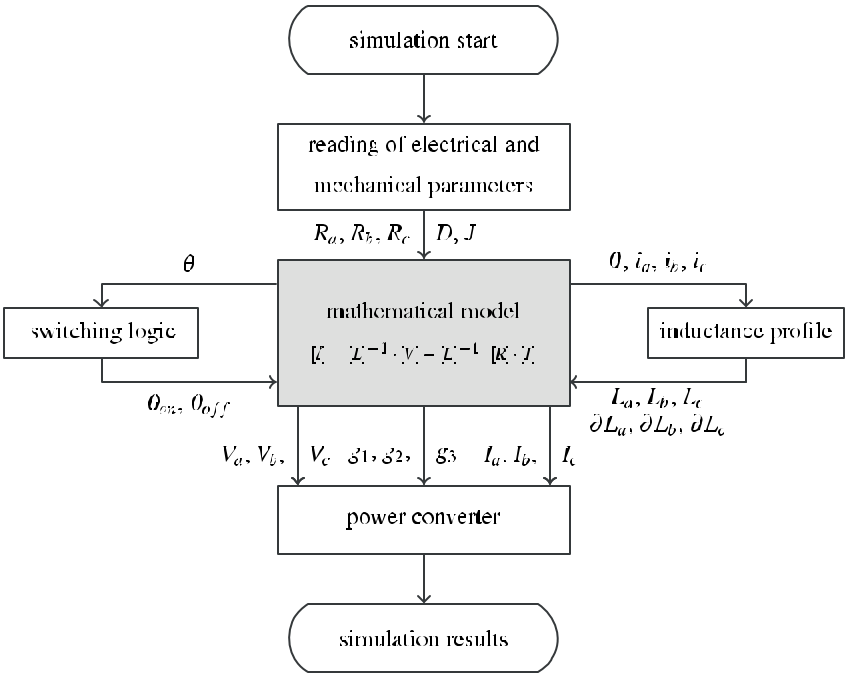

Fig. 2. Block diagram of the SRM simulation using the mathematical model.

model, is the interpolated model. In the interpolated model, the polynomial interpolation is performed on the inductance value (Kazmierkowski et al., 2002; Viajante et al., 2013). This procedure seeks to smooth the inductance curve and provide better simulation results. However, there is a high computational effort, greatly increasing the simulation time (Araujo et al., 2017).

3. Methodology

The purposes of this work are: (i) to present an alternative model to the methods that represent the SRM inductance profile, (ii) to submit the SRM to speed control using the classical Proportional, Integral and Derivative (PID) controller and (iii) perform the speed control through the switch-off angle of the half-bridge converter switches.

3.1. Proposed model for the inductance profile by parametric regression

In order to achieve the first objective the optimization process is used associated with the system identification technique known as parametric regression (Araujo et al., 2017; Gomes et al., 2017). The parametric regression process is the model fit that represents the system and this adjustment can happen empirically or optimally. In the empirical form, this adjustment is known as model synchronization, where the model outputs are compared to the system outputs (Soderstrom & Stoica, 1989). In the optimized parametric regression process the model and system output data are used as metrics for the optimization algorithm (Gomes et al., 2017).

As in the other nonlinear models that consider magnetic saturation, the proposed model depends on the experimental obtaining of inductance points for different values of angular position and current applied (Kazmierkowski et al., 2002; Silveira et al., 2009; Viajante et al., 2013). Unlike the Fourier series approximation model, the proposed model obtains the mathematical expression $L(\theta, i)$ representing the inductances of the machine under study.

To find the mathematical function corresponding to the machine inductance profile under study, it is necessary to perform the SRM test with locked rotor (Silveira et al., 2009). The test consists of choosing one of the phases randomly and using alternate current (AC) source to align the stator and rotor poles of this phase. The SRM rotor is locked and the position $\theta = 0°$ which is considered as maximum inductance. From this position, the rotor is locked at each position increment, where the variable source AC of frequency ϕ is used for winding excitation. Fig. 3(a) shows the electrical scheme used to obtain data set in locked rotor test. Fig. 3(b) illustrates inductance profile curves with addition of current value.

With the rotor locked at each position, the current is increased from *zero* to the maximum value supported by the machine at the manufacturing conditions or from *zero* to the approximate value at which the concatenated flow saturation is established. From the data collected experimentally: voltage V, current i, electrical resistance of R phase windings and frequency of applied AC voltage ϕ, the inductance is calculated, given by:

$$L = \left(\frac{V}{i}^2 - R^2\right)^{1/2} \cdot (2 \cdot \pi \cdot \phi)^{-1} \tag{11}$$

Thus, it is possible to know points of the phase inductance curves L for each applied current value i and rotor position θ, having a period of 90° for the 6 × 4 SRM, as presented in Gobbi, Rajendran, Ramar, Ahamed, and Anayet (2008) and Zhang, Cassani, and Williamson (2010). Given the inductance values obtained by (11), the parametric regression is used to find the mathematical expression representing the inductance surface $L_m(\theta, i)$. Unlike the other methods that represent the inductance profiles, the proposed method expresses the inductance profile, using the parametric regression method.

The parametric regression method is designed to be used in white box, gray box or black box systems and requires the values of input variables, system output values and mathematical model. In the specific case of this application, the system is gray box, because the mathematical model is defined in Araujo et al. (2017) and in Gomes et al. (2017). In the papers of Araujo et al. and Gomes et al. to find the surface $L_m(\theta, i)$ with characteristics of the inductance measured in the machine under study $L_e(\theta, i)$, is used (Araujo et al., 2017; Gomes et al., 2017):

$$L_m(\theta, i) = p_{(u)} + (f_1 \cdot f_2 \cdot f_3) \tag{12}$$

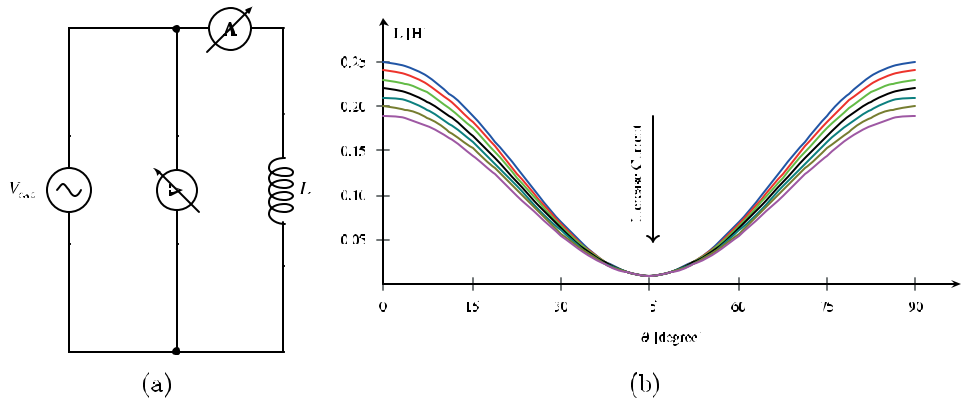

Fig. 3. Acquisition and inductance SRM profile: (a) electrical scheme for locked rotor assay and (b) theoretical inductance profile with the electrical current increase.

where f_1 is the expression defined in the Gaussian distribution that has parabolic behavior close to the origin and high continuity after the origin, f_2 is the expression defined in the Legendre polynomials that has behavior to adjust data of continuous functions and f_3 is the expression defined in the Fourier trigonometric series that has periodic behavior. These three models are associated because they are representative of the likely behavior of inductance surfaces.

Each of the expressions f_1, f_2 and f_3 represents a different behavior that can be altered by modifying the values of the coefficients, exponents and frequencies, given by:

$$f_1(\theta, i) = p_{(u+1)} \cdot e^{\left[p_{(u+2)} \cdot i + p_{(u+3)} \cdot \theta\right]} \tag{13}$$

$$f_2(\theta, i) = p_{(u+4)} \cdot i^{p_{(u+5)}} + p_{(u+6)} \cdot \theta^{p_{(u+7)}} + \cdots + p_{(v-3)} \cdot i^{p_{(v-2)}} + p_{(v-1)} \cdot \theta^{p_{(v)}} \tag{14}$$

$$\begin{aligned} f_3(\theta, i) = & p_{(w)} \cdot \sin\left[p_{(w+1)} \cdot i + p_{(w+2)}\right] \\ & + p_{(w+3)} \cdot \sin\left[p_{(w+4)} \cdot \theta + p_{(w+5)}\right] + \cdots \\ & + p_{(j-5)} \cdot \sin\left[p_{(j-4)} \cdot i + p_{(j-3)}\right] + p_{(j-2)} \cdot \sin\left[p_{(j-1)} \cdot \theta + p_{(j)}\right] \end{aligned} \tag{15}$$

where $p_{(u)}$ to $p_{(u+3)}$ are parameters related to the Gaussian distribution, $p_{(u+4)}$ to $p_{(v)}$ are parameters related to Legendre polynomials with $1 \leq u \leq v$ and $p_{(w)}$ to $p_{(j)}$ are the parameters related to the trigonometric series with $1 \leq w \leq j$ and $j + v$ is the number of parameters to be optimized, i.e., are coefficients, exponents and frequencies that define the characteristics of $L_m(\theta, i)$. These parameters are unknown and the optimization method is used to find their values. The set of inductance data measured experimentally in (11) is organized so that L is represented in the matrix $L_e(\theta, i)$ of dimension $a_1 \times b_1$, consisting of the measured values of θ and i. The fitness function of the optimization method uses the expressions (11) and (12) to compare the obtained results. Fig. 4 shows the flowchart of the parametric regression algorithm, where the region comprised by the dashed rectangle represents the model synchronization method proposed in Soderstrom and Stoica (1989) and the value $n_p = j + v$.

The matrices containing the system output data $L_e(\theta, i)$ and the model $L_m(\theta, i)$ have different dimensions and need to be normalized (in the block **normalization** Fig. 4) to be compared (in the block **comparison** Fig. 4).

The optimization process is performed through a hybrid algorithm, because it deals better with system with strong nonlinearity (Araujo et al., 2017). The hybrid algorithm used is the association of the deterministic Quasi-Newton method (QNM) with the heuristic method Genetic Algorithm (GA). The GA starts the optimization process with

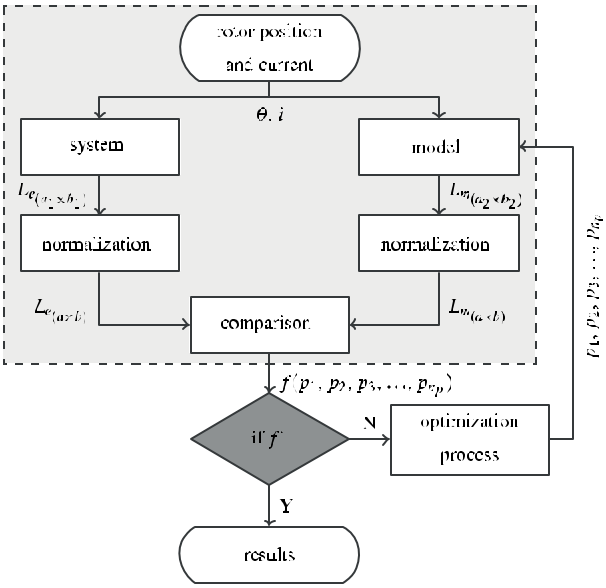

Fig. 4. Block diagram of the parametric regression algorithm.

random initial population and when it arrives the maximum generations established it delivers the best solution found for the QNM. The QNM completes its iterations, inserts its solution into the GA population, which restarts the optimization process until it stagnate, delivering its best solution back to the QNM (Gomes et al., 2017). This process is performed until one of the stop criteria is satisfied. The fitness function used in the optimization process is given by:

$$f_r\left(p_1, p_2, \ldots, p_{(n_p)}\right) = \frac{1}{4} \cdot \left(f_{a_r} + f_{a_r}\Big|_{\theta=0^\circ} + f_{a_r}\Big|_{\theta=90^\circ} + f_{a_r}\Big|_{33^\circ \leq \theta \leq 56^\circ}\right) \tag{16}$$

where,

$$f_{a_r}\left(p_1, p_2, \ldots, p_{(n_p)}\right) = \int_0^i \int_0^\theta \left|\frac{L_e(\theta, i) - L_m(\theta, i)}{L_e(\theta, i)}\right| d\theta di \tag{17}$$

where f_{a_r} is the difference between the surfaces $L_m(\theta, i)$ and $L_e(\theta, i)$. Some regions of the surface $L_m(\theta, i)$ were prioritized to obtain better adjustments, these regions are more important in the characterization of the SRM inductance. In this way, the regions (i) $\theta = 0°$, (ii) $\theta = 90°$ and (iii) $33° \leq \theta \leq 56°$, defined in (16), receive larger weights in the optimization process (Araujo et al., 2017; Gomes et al., 2017).

3.2. Speed control by excitation voltage with fixed switching angles

In order to achieve the second objective, the SRM is subjected to speed control using the classical Proportional, Integral and Derivative (PID) controller. The PID controller is chosen for simplicity in implementation and because it is an tool of low computational effort (N.d.S., 2010; Zheng et al., 2009). The SRM computational model is developed as shown in Fig. 2 and use the parametric regression inductance profile, all shown in Fig. 5 by the switched reluctance motor blocks, **inductance** and **switching logic**.

In the SRM simulation model, computational routines that are essential for drive modeling and control are added. They are: (i) AC–DC converter representing the fully controlled three-phase rectifier, (ii) PID controller and (iii) hysteresis controller (Araujo, 2006; Ogata, 2009; Viajante et al., 2013). In this way it is possible to perform speed control through the conduction angle of the electronic switches α of the AC-DC converter, represented in Fig. 5 by the highlighted black line. The speed control signal α, represented in Fig. 5 by the red line, acts directly on the SRM excitation voltage V_{exc} (Gomes et al., 2017; Rashid, 2014; Reis et al., 2013).

With the switching angles fixed in the half-bridge converter, the conduction window of the current in the coil is maintained at 30°, as recommended by the literature (Andrade & Krishnan, 2001; Kazmierkowski et al., 2002; Viajante et al., 2013). In this case, current hysteresis control is used to prevent the current in the coils from exceeding limit values and the drive is destructive to the machine. With reference to the peak current $I_{p_{ref}}$, the control signal of the hysteresis controller S_I is multiplied by the switch signal of the upper switches $S_{\theta_{off}}$ of the half-bridge, produced in the **switching logic** block, resulting in the signal applied to gates $G_{Q_{n_c}}$.

The PID controller is a linear model applied to a nonlinear system, so it is necessary to establish the control point for $\omega_{ref}(t)$ and then set the gain adjustment k_p, k_i and k_d of the driver. Several methods of adjustment of the PID controller are found in literature (Ogata, 2009; Reis, Araujo, Calixto, & Alves, 2015). Among the adjustment methods, those using an optimization process are frequently used because they present better responses when: (i) the machine operates with no load, (ii) with mechanical load insertion in the motor axis and (iii) the setpoint variation (Ogata, 2009; Reis et al., 2013).

Therefore, as a proposal of this work, the hybrid algorithm GA with QNM is used in the optimization process, and the fitness function that define the best speed adjustment is given by:

$$f_\omega\left(k_p, k_i, k_d\right) = \frac{1}{3}\cdot\left(\int_0^\infty \left|\frac{e_\omega(t)}{\omega_{ref}(t)}\right| dt + \left|\frac{\omega(t_M)-\omega(\infty)+e_\omega(\infty)}{\omega_{ref}(\infty)}\right|\right) \tag{18}$$

where t_M is the instant that ω has a maximum value in t. The expression (18) defines the normalized minimization referring to the error area represented by the integral of the absolute error (IAE), the percentage of exceeded represented by $\omega(t_M)-\omega(\infty)$ and the error in steady state represented by $e_\omega(\infty)$.The optimization process ensures optimal response to the control system. In this process, the parameters k_p, k_i and k_d can even be overridden by the optimization process, which can lead to controllers without one of the actions, such as: (i) P, (ii) PI, (iii) PD or (iv) PID. With the controller gains found by the optimizer it is necessary to perform tests, applying perturbations to the system, checking the control performance.

3.3. Speed control by switching angles with fixed excitation voltage

In order to reach the third objective, different speed controls topologies for the SRM are analyzed, enabling a comparative study of the control conditions, energy efficiency, electric current ripples, mechanical torque, electrical and mechanical power. In this case, the speed control is performed through the switch-off angle of the half-bridge converter $S_{\theta_{off}}$, where the firing angle α of the AC-DC converter switches is fixed, ensuring constant excitation voltage V_{exc}. Fig. 6 illustrates the control topology operating at $S_{\theta_{off}}$, where the speed control is represented by the highlighted black line acting directly on the reference current of the coils I_{ref} represented in the mesh by the red color line.

The PID speed controller acts directly on the reference current I_{ref} of the hysteresis controller. The current in the coil must be controlled during switching using the soft chopping technique, according Araujo (2006) the soft chopping technique provides lower ripple levels on phase current. However, losses switching remain, but are smaller in comparison to the hard chopping technique (without phase current control). Thus, the hysteresis control is used to ensure that the motor starting and operation current does not exceed rated values. In this control technique is expected that vibrations and torque ripples for high velocities are minimized (Araujo, 2006; Silveira et al., 2009; Viajante et al., 2013). Several studies indicate that the use of control by the coil disconnection angle may be detrimental to SRM energy efficiency Reis et al. (2015). This is another aspect to be analyzed.

3.4. Assisted speed control by excitation voltage with dynamic switching angles

In order to obtain greater performance of speed control and energetic efficiency, the control is used acting on the excitation voltage with proposals of non conventional adaptations. According to studies carried out in Reis et al. (2015), the control acting on the excitation voltage of the SRM produces greater energy efficiency. In addition, other studies have shown that for each value of ω there are turn on and turn off angles of the coils θ_{on} and θ_{off} which provide the highest efficiency (Reis, Araujo, & Calixto, 2017).

The behaviors of the relationships between θ_{on}, θ_{off} and ω that produce greater energy efficiency depend on the design features of the SRM (Araujo, 2006; Kazmierkowski et al., 2002; Silveira et al., 2009). However, there is no record of an analytical relationship for these quantities in the literature. In this way, the study is proposed aiming to maximize the energy efficiency η and to assure greater performance of control in a certain range of operation. This model is illustrated in Fig. 7, where the highlighted black line represents the speed control, with control signal represented by the red line. Still in Fig. 7, the gray blocks represent the proposed system for dynamic adjustment of both speed controller and switching angles.

It is applied to speed reference range model $\omega_{ref_{\min}} \le \omega_{ref} \le \omega_{ref_{\max}}$, considering that $\omega_{ref}(\infty) \cong \omega(\infty)$ under control conditions and for each ω_{ref} there is $\theta_{on_{\min}} \le \theta_{on} \le \theta_{on_{\max}}$ and $\theta_{off_{\min}} \le \theta_{off} \le \theta_{off_{\max}}$. Thus, the data set $\theta_{on}(\omega_{ref})$ and $\theta_{off}(\omega_{ref})$ that produce the highest energy efficiency are built. The parametric regression method is applied to find the coefficients of Legendre's polynomial $x_0, x_1, x_2, \ldots, x_n$ that represents $\theta_{on}(\omega_{ref})$ and $y_0, y_1, y_2, \ldots, y_n$ that represents $\theta_{off}(\omega_{ref})$, given by Gomes et al. (2017):

$$\theta_{on}(\omega_{ref}) = x_0 + x_1\cdot\omega_{ref} + x_2\cdot\omega_{ref}^2 + \cdots + x_n\cdot\omega_{ref}^n \tag{19}$$

$$\theta_{off}(\omega_{ref}) = y_0 + y_1\cdot\omega_{ref} + y_2\cdot\omega_{ref}^2 + \cdots + y_n\cdot\omega_{ref}^n \tag{20}$$

where n is the amount of coefficients required for optimum curve fit. Since the values of switching angles for this case are dynamic, the system where input is α and output is ω will also be changed dynamically. For the PID controller to act optimally at entire operating range $\omega_{ref_{\min}} \le \omega_{ref} \le \omega_{ref_{\max}}$, the hybrid optimization algorithm searches for optimized gains k_p, k_i and k_d with the empty system $T_m = 0$ for each ω_{ref}, using fitness function (18) .

Then the hybrid algorithm searches for the additional gains $k_{p_{Add}}$, $k_{i_{Add}}$ and $k_{d_{Add}}$ with the system under mechanical load insertion $T_{mag} > 0$. So T_m is calculated dynamically with the mechanical load observation

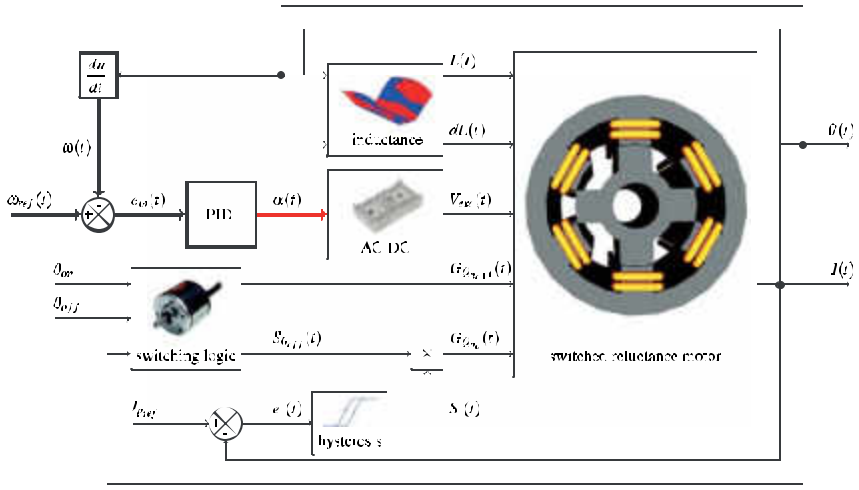

Fig. 5. Block diagram of the simulation for speed control system by excitation voltage with fixed switching angles.

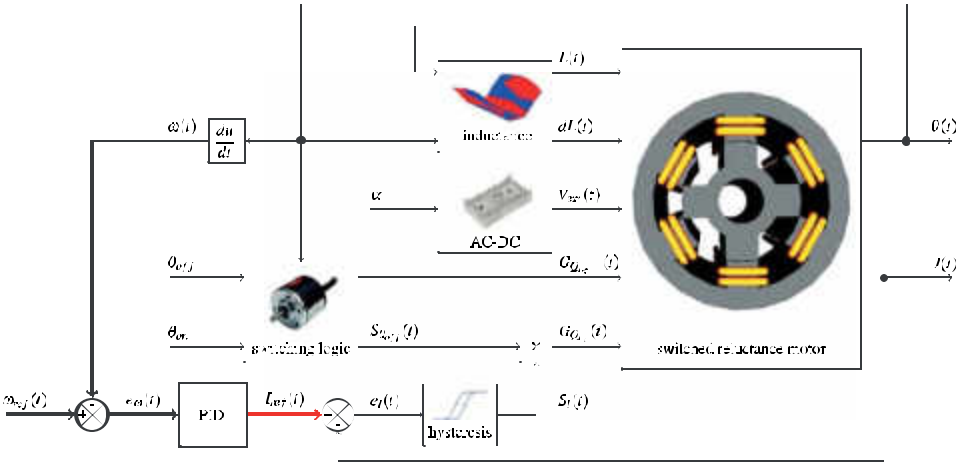

Fig. 6. Block diagram of the simulation for speed control system by switching angles with fixed excitation voltage.

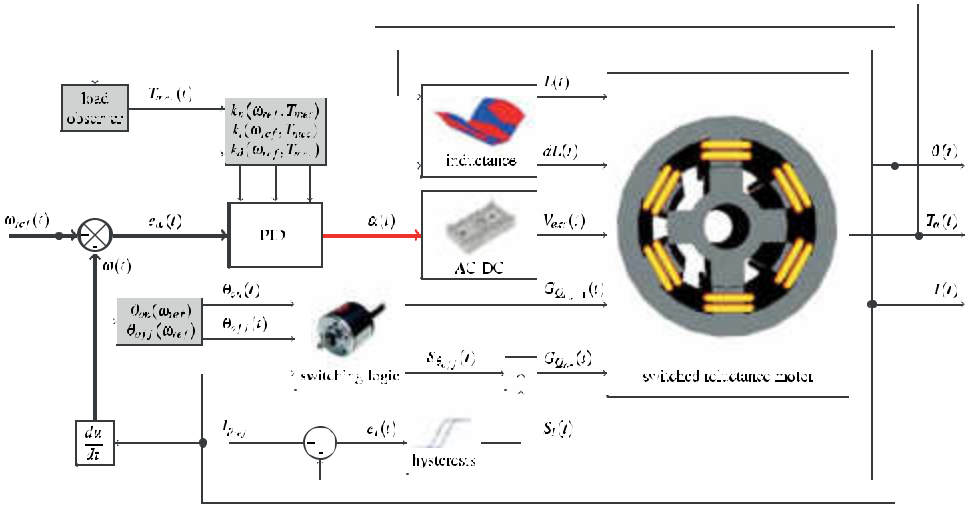

Fig. 7. Block diagram of the simulation for speed control system by excitation voltage with dynamic switching angles to efficiency improvement.

system applied to the SRM axis, using the expression (3). The parametric regression method is used to find the mathematical expression that best fits the data set of the gains for entire range $\omega_{ref_{\min}} \leq \omega_{ref} \leq \omega_{ref_{\max}}$. The expressions from (21) to (23) correspond to Legendre polynomial bases for the curve fitting relating to sets $k_p(\omega_{ref}, T_m)$, $k_i(\omega_{ref}, T_m)$ e $k_d(\omega_{ref}, T_m)$.

$$k_p(\omega_{ref}, T_m) = \underbrace{(A_0 + A_1 \cdot \omega_{ref} + A_2 \cdot \omega_{ref}^2 + \cdots + A_n \cdot \omega_{ref}^n)}_{\text{Proportional Gain } k_p} + \underbrace{(a_0 + a_1 \cdot \omega_{ref} + a_2 \cdot \omega_{ref}^2 + \cdots + a_m \cdot \omega_{ref}^m) \cdot T_m}_{\text{Additional Proportional Gain } k_{p_{Add}}} \tag{21}$$

$$k_i(\omega_{ref}, T_m) = \underbrace{(B_0 + B_1 \cdot \omega_{ref} + B_2 \cdot \omega_{ref}^2 + \cdots + B_n \cdot \omega_{ref}^n)}_{\text{Integral Gain } k_i} + \underbrace{(b_0 + b_1 \cdot \omega_{ref} + b_2 \cdot \omega_{ref}^2 + \cdots + b_m \cdot \omega_{ref}^m) \cdot T_m}_{\text{Additional Integral Gain } k_{i_{Add}}} \tag{22}$$

$$k_d(\omega_{ref}, T_m) = \underbrace{(C_0 + C_1 \cdot \omega_{ref} + C_2 \cdot \omega_{ref}^2 + \cdots + C_n \cdot \omega_{ref}^n)}_{\text{Derivative Gain } k_d} + \underbrace{(c_0 + c_1 \cdot \omega_{ref} + c_2 \cdot \omega_{ref}^2 + \cdots + c_m \cdot \omega_{ref}^m) \cdot T_m}_{\text{Additional Derivative Gain } k_{d_{Add}}} \tag{23}$$

where n and m are numbers of coefficients required for optimum curve fit. In this way, the system calculates the values of θ_{on} and θ_{off} which produce the highest energy efficiency and the values of $k_p(\omega_{ref}, T_m)$, $k_i(\omega_{ref}, T_m)$ and $k_d(\omega_{ref}, T_m)$ which produce the speed control greatest performance.

4. Results

In this work, four case studies are proposed with the following purposes: (i) construction of a mathematical and computational reliability model for the development of SRM drive and control techniques, (ii) conventional SRM drive keeping the coil switching angles fixed with control of speed and acting on the excitation voltage, (iii) conventional SRM drive maintaining the fixed excitation voltage with speed control and acting on the coil switching angles and (iv) unconventional SRM drive with coil switching angles and control dynamic speed, ensuring optimum adjustment over a wide speed range.

The results obtained from the proposed methodology used the computational model validated in other works (Andrade & Krishnan, 2001; Araujo et al., 2017). Thus, the simulations performed accurately represent the experimental setup built for the purpose of studies of drive and control techniques. The experimental setup is generic for the switched reluctance machine to operate as a motor and generator. In this way, a three-phase induction motor (IM) with cage rotor was coupled to the SRM axis. When the drive is realized for electric power production, IM acts as the primary machine and when the drive is performed for mechanical energy production, IM acts as an electromechanical brake.

In this work, the switched reluctance machine operates as a motor. The SRM used was designed using the finite element method and constructed manually (Araujo, 2006). The electromechanical parameters are presented by Table 2. These parameters are required for the computational model. Fig. 8 presents the experimental setup and its equipments are described in works (Araujo, 2006; Reis et al., 2013; Silveira et al., 2009).

4.1. Nonlinear model using induction profile found by parametric regression

The first result is related to finding the expression that best suits the profile of SRM inductance surface under study. For this, bench tests are performed by applying AC voltage on the phase A coil. The machine rotor has been blocked and the AC voltage has been increased in order to change the current value, until the saturation of magnetic flux begins. The current was varied from 0.5 A to 6 A, in rotor positions varying from 0° to 90°, increasing every 3°. The voltage and current AC values were applied in the expression (11), being $\phi = 60$ Hz and $R = 3.25\ \Omega$. The values of experimental inductances $L_e(\theta, i)$ are shown on the blue surface of Fig. 9(a).

Table 2
Parameters of the SRM used in this work.

Parameter	Value
Number of phases [phases]	3
Number of stator poles [poles]	6
Number of rotor poles [poles]	4
Phase resistance [Ω]	3.11
Inertia [(N m s^2)/rad]	$1.601 \cdot 10^{-2}$
Viscous friction [(N m s)/rad]	$1.656 \cdot 10^{-3}$
Rated voltage [V]	180
Rated current [A]	3.20
Aligned inductance [mH]	255
Unaligned inductance [mH]	32

From the experimental inductance data set $L_e(\theta, i)$ obtained by the test and by (11), the parametric regression algorithm was executed with values of $0° \leq \theta \leq 90°$ and $0.5\ \text{A} \leq i \leq 6\ \text{A}$ to find p parameters of expression (12). The hybrid algorithm was configured with the GA having a population of 20 individuals, maximum value of 100 generations, uniform mutation, tournament selection and heuristic crossover. The stopping criterion for iterations involves the maximum number of generations or when the fitness function reaches zero. (Gomes et al., 2017; Reis et al., 2013). The parameters p were found by the hybrid algorithm and the function $L_m(\theta, i)$, which represents the inductance surface of the SRM is expressed by:

$$L(\theta, i) = 1.10 + (\alpha \cdot \beta \cdot \gamma) \tag{24}$$

where α, β and γ are given from (25) to (27).

$$\alpha(\theta, i) = 3.41 \cdot 10^{-2} \cdot e^{[(-2.71 \cdot 10^{-1} \cdot i) - (2.76 \cdot 10^{-4} \cdot \theta)]} \tag{25}$$

$$\begin{aligned} \beta(\theta, i) &= 6.29 \cdot i^{9.22 \cdot 10^{-1}} + 1.52 \cdot 10^{-5} \cdot \theta^{(8.39 \cdot 10^{-4})} - 3.91 \cdot 10^{-1} \cdot i^{0.48} \\ &+ 2.03 \cdot 10^{-1} \cdot \theta^{(-5.97 \cdot 10^{-6})} + 1.88 \cdot 10^{-2} \cdot \theta^{8.97} - 0.84 \cdot i^{5.30 \cdot 10^{-1}} \end{aligned} \tag{26}$$

$$\begin{aligned} \gamma(\theta, i) &= 3.01 \cdot 10^{-1} \cdot \sin(1.42 \cdot 10^{-1} \cdot i + 5.51 \cdot 10^{-1}) \\ &+ 7.90 \cdot 10^{-1} \cdot \sin(4.37 \cdot 10^{-2} \cdot \theta + 2.48) \\ &+ 1.45 \cdot 10^{-1} \cdot \sin(4.92 \cdot 10^{-1} \cdot i + 4.95 \cdot 10^{-8}) \\ &- 1.80 \cdot 10^{-1} \cdot \sin(4.23 \cdot 10^{-2} \cdot \theta + 1.53) \\ &- 4.70 \cdot 10^{-2} \cdot \sin(4.81 \cdot 10^{-1} \cdot i - 1.50 \cdot 10^{-1}) \\ &+ 4.32 \cdot 10^{-2} \cdot \sin(1.72 \cdot 10^{-1} \cdot \theta + 5.96) \end{aligned} \tag{27}$$

The derivatives of inductances in function of θ are given by:

$$\begin{aligned} \frac{\partial L(\theta, i)}{\partial \theta} &= \alpha \cdot \{[3.41 \cdot 10^{-2} \cdot \cos(4.30 \cdot 10^{-2} \cdot \theta + 2.48) \\ &- 7.95 \cdot 10^{-3} \cdot \cos(4.22 \cdot 10^{-2} \cdot \theta + 1.53) \\ &+ 7.68 \cdot 10^{-3} \cdot \cos(1.71 \cdot 10^{-1} \cdot \theta + 5.96)] \cdot \beta \\ &- \alpha \cdot [1.60 \cdot 10^{-1} \cdot \theta^{-9.97} - 1.27 \cdot 10^{-8} \cdot \theta^{-9.90 \cdot 10^{-1}} + 1.23 \cdot 10^{-6} \cdot \theta^{-1}] \cdot \gamma \\ &- 9.43 \cdot 10^{-6} \cdot e^{[(-2.71 \cdot 10^{-1} \cdot i) - (2.76 \cdot 10^{-1} \cdot \theta)]} \cdot \beta \cdot \gamma\} \end{aligned} \tag{28}$$

The optimizer provided a fitness function of $f_r = 0.117\%$ for parametric regression, $f_r = 0.691\%$ for the Fourier method and $f_r = 0.725\%$ for the interpolated Fourier method, thus guaranteeing optimized values. Fig. 9 shows the inductances obtained by the interpolated parametric, Fourier and Fourier regression. The regions considered by

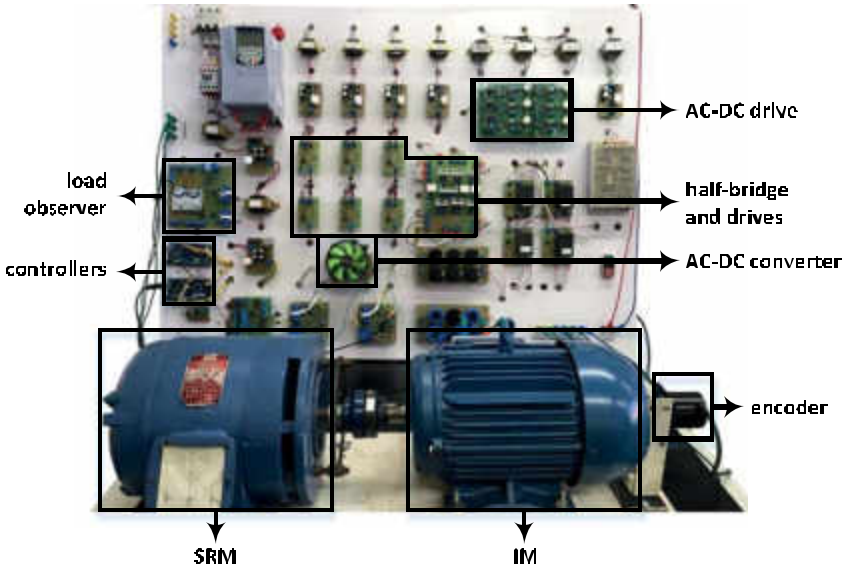

Fig. 8. Experimental setup developed in laboratory to operation of the SRM.

Table 3
Comparison between the models: parametric regression, Fourier and interpolated Fourier.

		f_{a_r} [%]				
Simulation	f_r [%]	all θ	$\theta = 0°$	$\theta = 90°$	$33° \leq \theta \leq 56°$	T_s [s]
Regression	0.117	0.301	0.023	0.027	0.116	0.030
Fourier	0.691	0.392	1.138	1.138	0.097	0.272
Interpolated	0.490	0.422	0.710	0.710	0.118	33.730

the evaluation function, given by (16), obtained error values for all θ and i of parametric regression $f_{a_r} = 0.301\%$, for Fourier method $f_{a_r} = 0.392\%$ and for interpolated Fourier method $f_{a_r} = 0.478\%$, represented by the surfaces of Figs. 9(a)–9(c) respectively.

The region in which $\theta = 0°$, the error obtained for the parametric regression was $f_{a_r} = 0.023\%$, for the Fourier method $f_{a_r} = 1.138\%$ and for the interpolated Fourier method $f_{a_r} = 1.046\%$, represented by Figure 9(d). The region in which $\theta = 90°$, the error obtained for the parametric regression was $f_{a_r} = 0.027\%$, for the Fourier method $f_{a_r} = 1.138\%$ and for the interpolated Fourier method $f_{a_r} = 1.046\%$, represented by Fig. 9(e). The region where $33° \leq \theta \leq 56°$ the parametric regression error was $f_{a_r} = 0.116\%$, for Fourier method $f_{a_r} = 0.097\%$ and for interpolated Fourier method $f_{a_r} = 0.333\%$, represented by Fig. 9(f). The results described and the calculation time for 1 s of simulation T_s, on a i7-7700HQ 2.8 GHz with 32GB RAM DDR4 2400MHz computer, are present in Table 3.

To obtain greater accuracy in the region where $33° \leq \theta \leq 56°$, the parametric regression algorithm can be run with other optimization methods, but the computational effort will be greater.

The proposed parametric regression model finds the corresponding expression of SRM inductance surface under study and this inductance profile can be applied in simulation, providing studies of techniques to improve the SRM drive and control.

This modeling is necessary to obtain an approximate representation of the experimental system, providing the analysis of the model in different case studies of SRM drive and control.

4.2. Case study I: speed control by excitation voltage with fixed switching angles

Using the inductance profile found by the parametric regression, the SRM is submitted to speed control as proposed in topology of Fig. 5. For this case, the reference peak current is set at $I_{p_{ref}} = 15$ A and switching angles are those recommended by the literature $\theta_{on} = 0°$ and $\theta_{off} = 30°$. A step signal was applied at speed reference $\omega_{ref} = 150$ rad/s with applied load torque $T_L = 5$ N m at $t = 7$ s. The hybrid algorithm is used to find the gains of PID controller. The fitness function used is given by (18) and the gains found are $k_p = 2.291 \cdot 10^{-1}$ [° s/rad], $k_i = 2.983 \cdot 10^{-1}$ [° s/rad] and $k_d = 7.988 \cdot 10^{-5}$ [° s/rad]. Fig. 10 presents the results with optimized PID controller acting on excitation voltage with fixed switching angles.

The value of optimization process fitness function that found PID controller gains is $f_\omega = 3.01\%$. Fig. 10(b) shows the peak current during SRM startup which was approximately $I_p \approx 15A$ and after insertion of mechanical load of $I_p \approx 7A$. The average torque developed by SRM is $T_m \approx 5.15$ N m and the torque ripple $r_T \approx 6.9$ N m as shown in Fig. 10(c). In Fig. 10(d) the average electrical power consumed is $P_e \approx 1004W$ and the average power converted into mechanical power delivered by SRM is approximately $P_m \approx 756W$.For this case, the excitation voltage applied in DC bus by PID controller was $V_{exc} \approx 253V$, average voltage and current in coil was respectively $V_{avg} \approx 115V$ and $I_{avg} \approx 2.15A$, not exceeding the nominal values of the machine presented in Table 2.

The energy efficiency of SRM for this case study is $\eta \approx 0.753$, as shown in Fig. 10(d), when mechanical load is applied to the shaft. The study was performed considering conventional drive with control acting on excitation voltage and windowed switching angles of 30°. In this case the system presented speed control response with correction after the insertion of mechanical load, with time less than 5s and energy efficiency within the standards, considering that machine used was built by hand Araujo (2006). In the next case study, the speed control of the SRM is performed keeping the excitation voltage fixed, acting only at the switching angles.

4.3. Case study II: speed control by switching angles with fixed excitation voltage

In this case study the SRM was submitted to speed control using topology proposed in Fig. 6. Thus, the excitation voltage was set at $V_{exc} = 525V$ and the switching angles are those recommended by the literature $\theta_{on} = 0°$ and $\theta_{off} = 30°$. A step signal was applied with the following parameter values: $\omega_{ref} = 150$ rad/s, $T_L = 5$ N m at $t = 7$ s. The hybrid algorithm with fitness function given by (18) was used to find the gains of PID controller, where the gains found

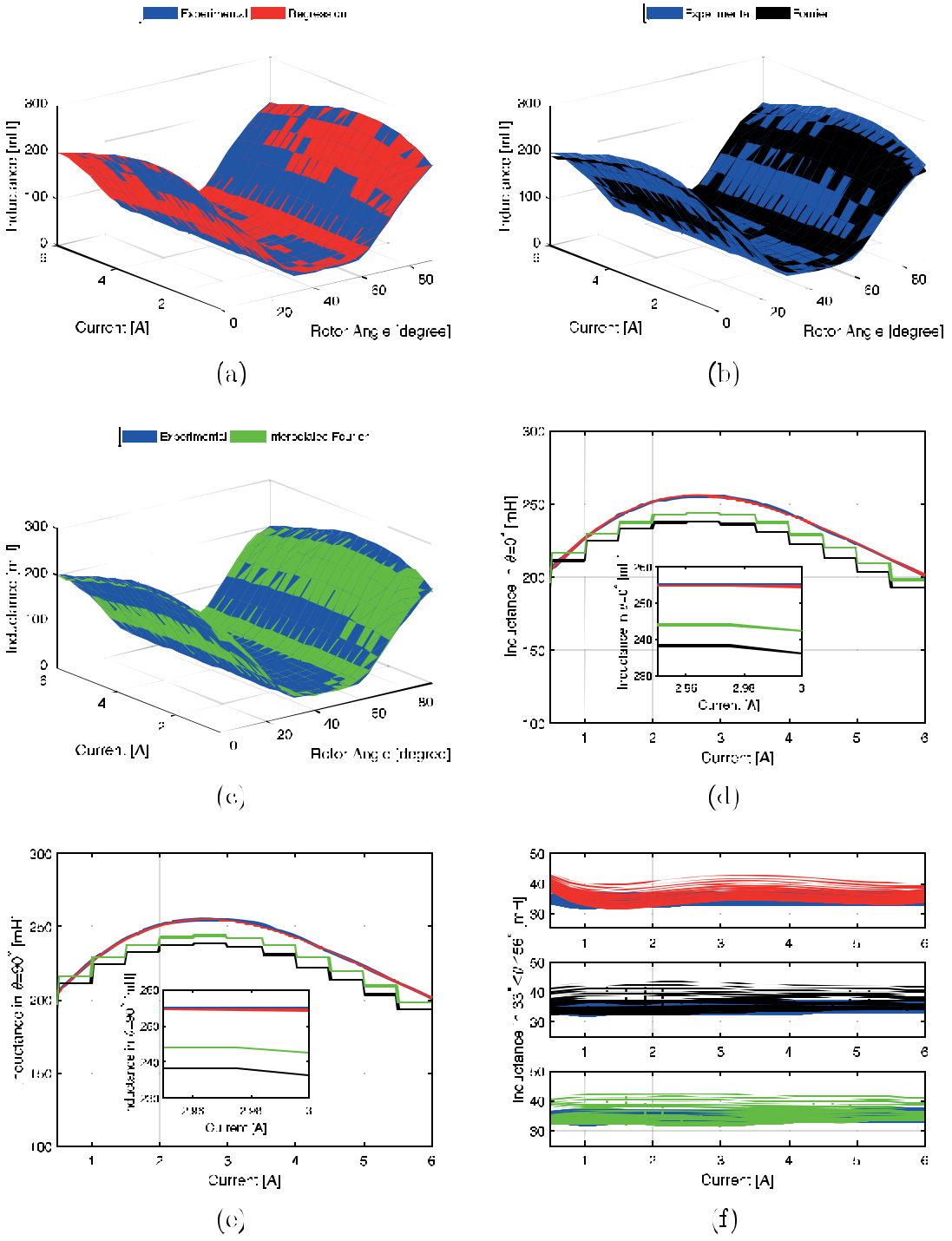

Fig. 9. Inductance profile: (a) inductance surface for parametric regression and experimental, (b) inductance surface for Fourier and experimental, (c) inductance surface for interpolated Fourier and experimental, (d) inductances in $\theta = 0°$, (e) inductances in $\theta = 90°$ and (f) inductances in $33° \leq \theta \leq 56°$.

are: $k_p = 8.084 \cdot 10^{-2}$ [A s/rad], $k_i = 8.784 \cdot 10^{-2}$ [A s/rad] and $k_d = 7.779 \cdot 10^{-6}$ [A s/rad]. Fig. 11 presents the results with optimized PID controller acting on the coil current through switching angles.

The fitness function of optimization process that found the gains of PID controller is $f_\omega = 6.06\%$. Fig. 11(b) shows the peak current during SRM startup of less than 15 A and after insertion of mechanical load of $I_p \approx 7$ A. The average torque developed by the SRM was $T_m \approx 5.13$ N m and the torque ripple of $r_T \approx 7.25$ N m, as shown in Fig. 11(c). In Fig. 11(d) the average electrical power consumed is $P_e \approx 1093$ W and the average power converted into mechanical power delivered by the SRM is approximately $P_m \approx 750$ W.

The SRM energy efficiency in this case study is $\eta \approx 0.686$, as shown in Fig. 11(d), when mechanical load is applied to the machine shaft. The study was performed considering the conventional drive with control acting on reference current by switching the coils with a fixed conduction window at 30°. In this case, the system presented speed

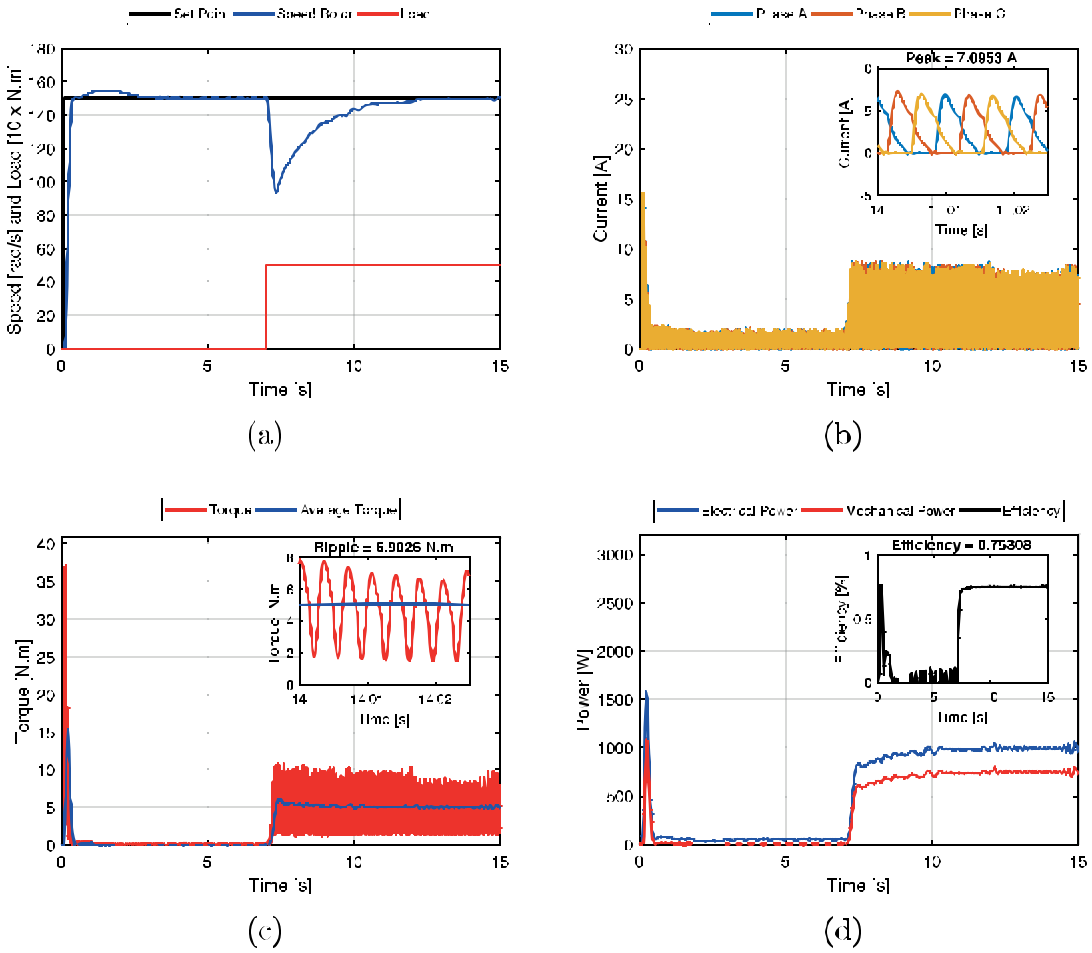

Fig. 10. PID controller optimization acting on the excitation voltage with fixed switching angles: (a) speed response for ω_{ref} = 150 rad/s, (b) current per phase, (c) SRM torque and (d) input electrical power, mechanical output power and SRM energy efficiency.

control response with correction after insertion of mechanical load in time less than 3.5 s and energy efficiency lower than the previous case in 8.9%. For this case, average voltage and current in coil were respectively $V_{avg} \approx 90$ V and $I_{avg} \approx 2.2$ A. For the last case study, SRM velocity control is performed by acting on both the excitation voltage and the switching angles, in order to analyze the performance of the SRM and compare with the previous case studies.

4.4. Case study III: assisted speed control by excitation voltage with dynamic switching angles to efficiency improvement

Based on the control loop in Fig. 7, it was performed a procedure to know θ_{on} and θ_{off} which provide greater efficiency of SRM for each ω_{ref} with T_L = 5 N m. The test consists of incrementing switching angles from $-5° \leq \theta_{on} \leq 15°$ and $-20° \leq \theta_{off} \leq 40°$, with 2° range, for each speed 50 rad/s $\leq \omega_{ref} \leq$ 150 rad/s, with a 5 rad/s range. For this analysis, PID controller parameters used are the same as those found by hybrid algorithm in Case Study I.

Thus, the values of θ_{on} and θ_{off} which produce the highest energy efficiency for each velocity are shown in Fig. 12(a). The values of θ_{on} would remain constant for all speeds, in this case in (19), $\theta_{on}(\omega_{ref}) = 10.75°$. Since the values of θ_{off} are dynamic as a function of speed, the least squares method was used to find expression coefficients (20) that fit the blue curve of Fig. 12(a).

Tests were performed using the least square method with $1 \leq n \leq 50$ from (19) to (23), in order to find the value of n that provided optimized expression reducing the edge effect or Runge's phenomenon described in Gomes et al. (2017). The expression found using the proposed method is given by (29) and can be visualized by the red curve in Fig. 12(a).

$$\begin{aligned}\theta_{off}(\omega_{ref}) = & -1.052\cdot 10^{8} + 1.941\cdot 10^{7}\cdot\omega_{ref} \\ & - 1.660\cdot 10^{6}\cdot\omega_{ref}^{2} + 8.750\cdot 10^{4}\cdot\omega_{ref}^{3} \\ & - 3.177\cdot 10^{3}\cdot\omega_{ref}^{4} + 8.431\cdot 10^{1}\cdot\omega_{ref}^{5} \\ & - 1.691\cdot\omega_{ref}^{6} + 2.618\cdot 10^{-2}\cdot\omega_{ref}^{7} \\ & - 3.158\cdot 10^{-4}\cdot\omega_{ref}^{8} + 2.980\cdot 10^{-6}\cdot\omega_{ref}^{9} \\ & - 2.192\cdot 10^{-8}\cdot\omega_{ref}^{10} + 1.245\cdot 10^{-10}\cdot\omega_{ref}^{11} \\ & - 5.349\cdot 10^{-13}\cdot\omega_{ref}^{12} + 1.681\cdot 10^{-15}\cdot\omega_{ref}^{13} \\ & - 3.645\cdot 10^{-18}\cdot\omega_{ref}^{14} + 4.875\cdot 10^{-21}\cdot\omega_{ref}^{15} \\ & - 3.029\cdot 10^{-24}\cdot\omega_{ref}^{16} \end{aligned} \quad (29)$$

With the expression (29) found and inserted in model, PID controller with static gains will act in an optimized way, considering dynamic values of θ_{off}. In this way, static gains of PID controller are optimized for each speed with 50 rad/s $\leq \omega_{ref} \leq$ 150 rad/s, using hybrid algorithm with fitness function given by (18). In Fig. 12(b), Fig. 12(c) and Fig. 12(d) blue and black colors show the gain and additional results of PID controlled gains that provide optimized fit for entire 50 rad/s $\leq \omega_{ref} \leq$ 150 rad/s.

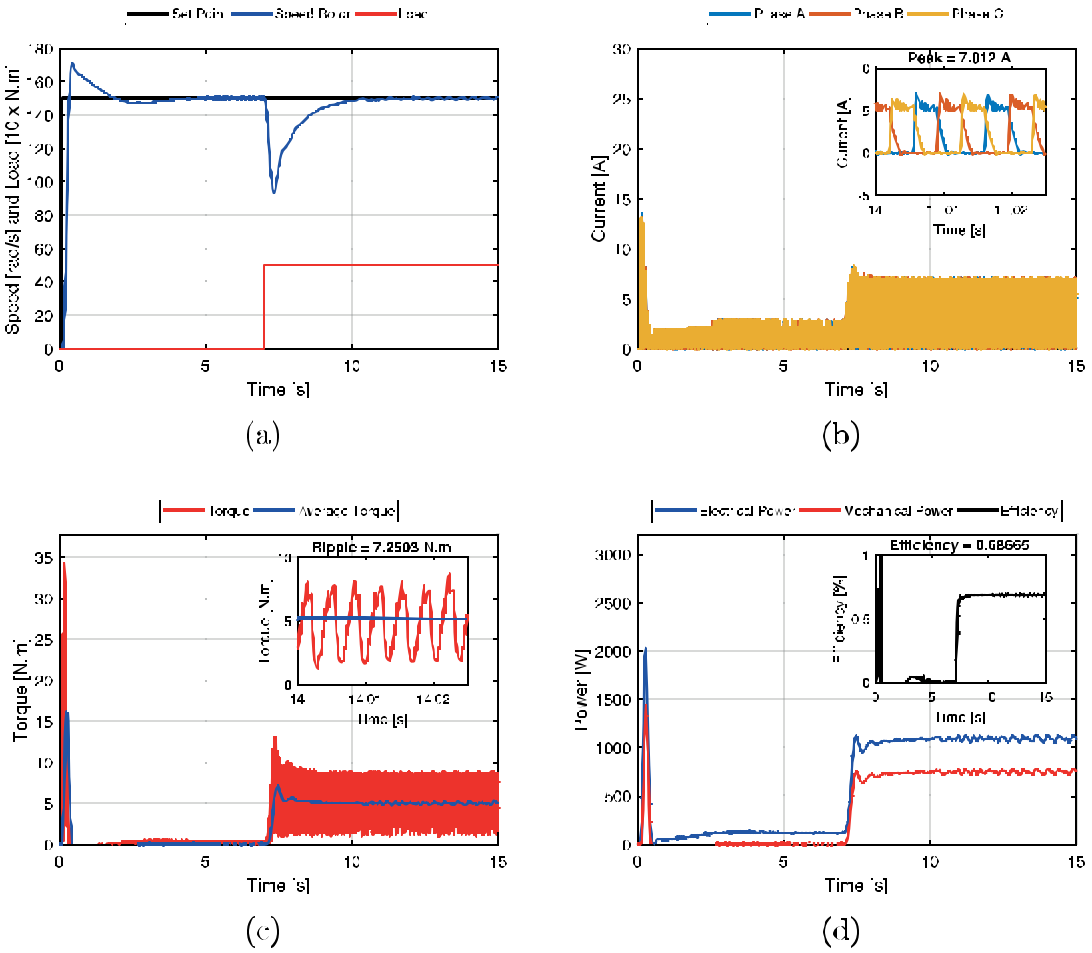

Fig. 11. PID controller optimization acting at the switching angles with fixed excitation voltage: (a) speed response for $\omega_{ref} = 150$ rad/s, (b) current per phase, (c) SRM torque and (d) input electrical power, mechanical output power and SRM energy efficiency.

With the values of gains and additional gains known, the least squares method was used to obtain expression that fits the gains found. The expressions bases for the curve fit are given by (21), (22) and (23). Tests were performed using the least squares, for $1 \leq n \leq 50$ and $1 \leq m \leq 50$, which would provide n and m for optimized expressions. The expressions found are given by (30), (31) and (32) and can be seen in Figs. 12(b)–12(d) in red colored lines.

$$
\begin{aligned}
k_p(\omega_{ref}, T_m) = \; & \big(+3.819\cdot 10^{3} - 5.777\cdot 10^{2}\cdot\omega_{ref} \\
& + 3.981\cdot 10^{1}\cdot\omega_{ref}^{2} - 1.655\omega_{ref}^{3} \\
& + 4.632\cdot 10^{-2}\cdot\omega_{ref}^{4} - 9.213\cdot 10^{-4}\cdot\omega_{ref}^{5} \\
& + 1.339\cdot 10^{-5}\cdot\omega_{ref}^{6} - 1.442\cdot 10^{-7}\cdot\omega_{ref}^{7} \\
& + 1.150\cdot 10^{-9}\cdot\omega_{ref}^{8} - 6.712\cdot 10^{-12}\cdot\omega_{ref}^{9} \\
& + 2.785\cdot 10^{-14}\cdot\omega_{ref}^{10} - 7.785\cdot 10^{-17}\cdot\omega_{ref}^{11} \\
& + 1.314\cdot 10^{-19}\cdot\omega_{ref}^{12} - 1.013\cdot 10^{-22}\cdot\omega_{ref}^{13}\big) \\
& + \big(2.739\cdot 10^{6} - 4.715\cdot 10^{5}\cdot\omega_{ref} \\
& + 3.625\cdot 10^{4}\cdot\omega_{ref}^{2} - 1.625\cdot 10^{3}\cdot\omega_{ref}^{3} \\
& + 4.638\cdot 10^{1}\cdot\omega_{ref}^{4} - 8.587\cdot 10^{-1}\cdot\omega_{ref}^{5} \\
& + 1.024\cdot 10^{-2}\cdot\omega_{ref}^{6} - 9.553\cdot 10^{-5}\cdot\omega_{ref}^{7} \\
& + 1.701\cdot 10^{-6}\cdot\omega_{ref}^{8} - 4.327\cdot 10^{-8}\cdot\omega_{ref}^{9} \\
& + 7.233\cdot 10^{-10}\cdot\omega_{ref}^{10} - 6.527\cdot 10^{-12}\cdot\omega_{ref}^{11} \\
& + 1.401\cdot 10^{-14}\cdot\omega_{ref}^{12} + 3.182\cdot 10^{-16}\cdot\omega_{ref}^{13} \\
& - 2.558\cdot 10^{18}\cdot\omega_{ref}^{14} - 1.236\cdot 10^{-20}\cdot\omega_{ref}^{15} \\
& + 2.937\cdot 10^{-22}\cdot\omega_{ref}^{16} - 1.414\cdot 10^{-24}\cdot\omega_{ref}^{17} \\
& - 3.611\cdot 10^{-27}\cdot\omega_{ref}^{18} + 5.350\cdot 10^{-29}\cdot\omega_{ref}^{19} \\
& + 4.978\cdot 10^{-32}\cdot\omega_{ref}^{20} - 2.758\cdot 10^{-33}\cdot\omega_{ref}^{21} \\
& + 1.290\cdot 10^{-35}\cdot\omega_{ref}^{22} + 9.233\cdot 10^{-39}\cdot\omega_{ref}^{23} \\
& - 3.185\cdot 10^{-40}\cdot\omega_{ref}^{24} + 1.366\cdot 10^{-42}\cdot\omega_{ref}^{25} - 2.677\cdot 10^{-45}\cdot\omega_{ref}^{26} \\
& + 2.120\cdot 10^{-48}\cdot\omega_{ref}^{27}\big)\cdot T_m
\end{aligned}
\tag{30}
$$

The expressions are inserted in developed computational model, proposed in Fig. 7, where SRM is subjected to speed control. For this case, reference peak current is set at $I_{p_{ref}} = 15A$ and switching angles are calculated dynamically according to (29). A step signal was applied at speed reference $\omega_{ref} = 150$ rad/s with applied load torque $T_L = 5$ N m at $t = 7$ s. The controller parameters are dynamically computed given by expressions from (30) to (32) and Fig. 13 presents the model results.

The fitness function value found by expression (18), for test where $\omega_{ref} = 150$ rad/s, is $f_\omega = 3.11\%$. Fig. 13(b) shows the peak current during SRM startup which was approximately $I_p \approx 15A$ and after insertion of mechanical load of $I_p \approx 7A$. The average torque developed by the SRM is $T_m \approx 5.18$ N m and the torque ripple of $r_T \approx 6.9$ N m, as shown in Fig. 13(c). In Fig. 13(d) the average electrical power consumed is $P_e \approx 988W$ and the average power converted into mechanical power delivered by SRM is approximately $P_m \approx 753W$. For this case, the excitation voltage applied to the DC bus of the machine was $V_{exc} \approx$

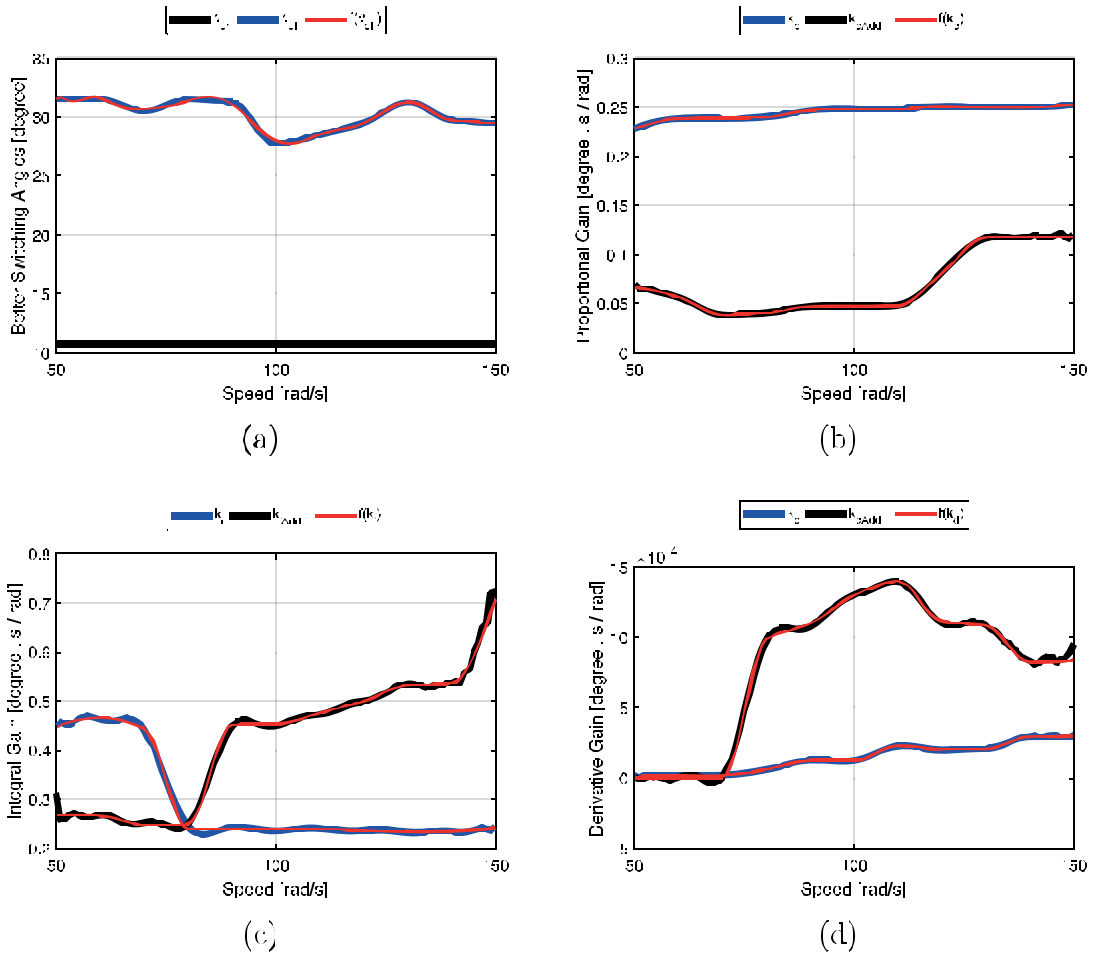

Fig. 12. Identification of expressions that represent the dynamics, as a function of speed, of switching angles and PID controller parameters: (a) SRM turn on angle, (b) PID controller proportional action, (c) PID controller integral action and (d) PID controller derivative action.

$253V$, resulting in average values of $V_{avg} \approx 115V$ for the voltage in the coil and $I_{avg} \approx 2.15A$ for the current in the coil. As shown in Fig. 13(d), the SRM energy efficiency for this case study is $\eta \approx 0.762$ when applied mechanical load on machine shaft.

$$
\begin{aligned}
k_i(\omega_{ref}, T_m) \;=\; & \big(-1.061\cdot 10^{7} + 2.007\cdot 10^{6}\cdot \omega_{ref} - 1.757\cdot 10^{5}\cdot \omega_{ref}^{2} \\
& + 9.444\cdot 10^{3}\cdot \omega_{ref}^{3} - 3.481\cdot 10^{2}\cdot \omega_{ref}^{4} + 9.310\cdot \omega_{ref}^{5} - 1.860\cdot 10^{-1}\cdot \omega_{ref}^{6} \\
& + 2.812\cdot 10^{-3}\cdot \omega_{ref}^{7} - 3.201\cdot 10^{-5}\cdot \omega_{ref}^{8} + 2.662\cdot 10^{-7}\cdot \omega_{ref}^{9} \\
& - 1.465\cdot 10^{-9}\cdot \omega_{ref}^{10} \\
& + 3.121\cdot 10^{-12}\cdot \omega_{ref}^{11} + 2.929\cdot 10^{-14}\cdot \omega_{ref}^{12} - 3.655\cdot 10^{-16}\cdot \omega_{ref}^{13} \\
& + 2.147\cdot 10^{-18}\cdot \omega_{ref}^{14} \\
& - 7.972\cdot 10^{-21}\cdot \omega_{ref}^{15} + 1.905\cdot 10^{-23}\cdot \omega_{ref}^{16} - 2.701\cdot 10^{-26}\cdot \omega_{ref}^{17} \\
& + 1.737\cdot 10^{-29}\cdot \omega_{ref}^{18}\big) \\
& - \big(1.443\cdot 10^{6} + 8.044\cdot 10^{5}\cdot \omega_{ref} - 1.141\cdot 10^{5}\cdot \omega_{ref}^{2} + 8.095\cdot 10^{3}\cdot \omega_{ref}^{3} \\
& - 3.434\cdot 10^{2}\cdot \omega_{ref}^{4} + 9.206\cdot \omega_{ref}^{5} - 1.500\cdot 10^{-1}\cdot \omega_{ref}^{6} + 1.097\cdot 10^{-3}\cdot \omega_{ref}^{7} \\
& + 8.055\cdot 10^{-6}\cdot \omega_{ref}^{8} - 2.350\cdot 10^{-7}\cdot \omega_{ref}^{9} + 4.161\cdot 10^{-10}\cdot \omega_{ref}^{10} \\
& + 4.566\cdot 10^{-11}\cdot \omega_{ref}^{11} \\
& - 7.411\cdot 10^{-13}\cdot \omega_{ref}^{12} + 4.834\cdot 10^{-15}\cdot \omega_{ref}^{13} - 3.387\cdot 10^{-18}\cdot \omega_{ref}^{14} \\
& - 1.164\cdot 10^{-19}\cdot \omega_{ref}^{15} \\
& - 6.489\cdot 10^{-23}\cdot \omega_{ref}^{16} + 1.009\cdot 10^{-23}\cdot \omega_{ref}^{17} - 9.150\cdot 10^{-26}\cdot \omega_{ref}^{18} \\
& + 6.783\cdot 10^{-28}\cdot \omega_{ref}^{19} \\
& - 4.860\cdot 10^{-30}\cdot \omega_{ref}^{20} + 1.759\cdot 10^{-32}\cdot \omega_{ref}^{21} + 5.013\cdot 10^{-35}\cdot \omega_{ref}^{22} \\
& - 8.470\cdot 10^{-37}\cdot \omega_{ref}^{23} \\
& + 6.192\cdot 10^{-39}\cdot \omega_{ref}^{24} - 4.486\cdot 10^{-41}\cdot \omega_{ref}^{25} + 1.977\cdot 10^{-43}\cdot \omega_{ref}^{26} \\
& - 4.518\cdot 10^{-46}\cdot \omega_{ref}^{27} \\
& + 8.257\cdot 10^{-48}\cdot \omega_{ref}^{28} - 1.212\cdot 10^{-49}\cdot \omega_{ref}^{29} + 7.969\cdot 10^{-52}\cdot \omega_{ref}^{30} \\
& - 2.701\cdot 10^{-54}\cdot \omega_{ref}^{31} \\
& + 4.400\cdot 10^{-57}\cdot \omega_{ref}^{32} - 1.594\cdot 10^{-60}\cdot \omega_{ref}^{33} - 2.767\cdot 10^{-63}\cdot \omega_{ref}^{34}\big)\cdot T_m
\end{aligned}
\tag{31}
$$

The study was performed considering unconventional drive with assisted control, acting on excitation voltage and dynamic switching angles. In this case, the system presented speed control response with correction after insertion of mechanical load in time of approximately $3s$ and superior energy efficiency at 1.12% with respect to the conventional Case Study I drive and 10% with respect to the drive presented in Case Study II. It is worth mentioning that the tests were performed at only one SRM operating point, where $\omega = 150$ rad/s and $T_L = 5$ N m.

$$
\begin{aligned}
k_d(\omega_{ref}, T_m) \;=\; & \big(-7.401\cdot 10^{3} + 1.410\cdot 10^{3}\cdot \omega_{ref} - 1.221\cdot 10^{2}\cdot \omega_{ref}^{2} \\
& + 6.334\cdot \omega_{ref}^{3} - 2.171\cdot 10^{-1}\cdot \omega_{ref}^{4} + 5.101\cdot 10^{-3}\cdot \omega_{ref}^{5} \\
& - 8.142\cdot 10^{-5}\cdot \omega_{ref}^{6} \\
& + 8.128\cdot 10^{-7}\cdot \omega_{ref}^{7} - 3.342\cdot 10^{-9}\cdot \omega_{ref}^{8} - 2.690\cdot 10^{-11}\cdot \omega_{ref}^{9} \\
& + 4.180\cdot 10^{-13}\cdot \omega_{ref}^{10}
\end{aligned}
$$

$$
\begin{aligned}
&- 9.386\cdot 10^{-16}\cdot\omega_{ref}^{11} - 1.404\cdot 10^{-17}\cdot\omega_{ref}^{12} + 3.476\cdot 10^{-20}\cdot\omega_{ref}^{13}\\
&+ 5.523\cdot 10^{-22}\cdot\omega_{ref}^{14}\\
&+ 7.743\cdot 10^{-24}\cdot\omega_{ref}^{15} + 1.600\cdot 10^{-25}\cdot\omega_{ref}^{16} + 3.069\cdot 10^{-28}\cdot\omega_{ref}^{17}\\
&+ 9.139\cdot 10^{-30}\cdot\omega_{ref}^{18}\\
&- 4.791\cdot 10^{-32}\cdot\omega_{ref}^{19} - 4.053\cdot 10^{-34}\cdot\omega_{ref}^{20} + 4.803\cdot 10^{-36}\cdot\omega_{ref}^{21}\\
&- 6.551\cdot 10^{-39}\cdot\omega_{ref}^{22}\\
&- 1.607\cdot 10^{-40}\cdot\omega_{ref}^{23} + 1.269\cdot 10^{-42}\cdot\omega_{ref}^{24} - 4.514\cdot 10^{-45}\cdot\omega_{ref}^{25}\\
&+ 8.292\cdot 10^{-48}\cdot\omega_{ref}^{26}\\
&- 6.401\cdot 10^{-51}\cdot\omega_{ref}^{27}\big)\\
&- \big(2.421\cdot 10^{5} + 4.830\cdot 10^{4}\cdot\omega_{ref} - 4.426\cdot 10^{3}\cdot\omega_{ref}^{2}\\
&+ 2.459\cdot 10^{2}\cdot\omega_{ref}^{3} - 9.207\cdot\omega_{ref}^{4}\\
&+ 2.429\cdot 10^{-1}\cdot\omega_{ref}^{5} - 4.568\cdot 10^{-3}\cdot\omega_{ref}^{6} + 5.950\cdot 10^{-5}\cdot\omega_{ref}^{7}\\
&- 4.774\cdot 10^{-7}\cdot\omega_{ref}^{8}\\
&+ 1.100\cdot 10^{-9}\cdot\omega_{ref}^{9} + 2.211\cdot 10^{-11}\cdot\omega_{ref}^{10} - 2.334\cdot 10^{-13}\cdot\omega_{ref}^{11}\\
&- 4.189\cdot 10^{-17}\cdot\omega_{ref}^{12}\\
&+ 1.717\cdot 10^{-17}\cdot\omega_{ref}^{13} - 1.186\cdot 10^{-19}\cdot\omega_{ref}^{14} - 9.644\cdot 10^{-23}\cdot\omega_{ref}^{15}\\
&+ 4.762\cdot 10^{-24}\cdot\omega_{ref}^{16}\\
&- 8.491\cdot 10^{-27}\cdot\omega_{ref}^{17} - 1.857\cdot 10^{-28}\cdot\omega_{ref}^{18} + 9.665\cdot 10^{-31}\cdot\omega_{ref}^{19}\\
&+ 5.310\cdot 10^{-33}\cdot\omega_{ref}^{20}\\
&- 8.318\cdot 10^{-35}\cdot\omega_{ref}^{21} + 4.482\cdot 10^{-37}\cdot\omega_{ref}^{22}\\
&- 1.319\cdot 10^{-39}\cdot\omega_{ref}^{23}\\
&+ 2.124\cdot 10^{-42}\cdot\omega_{ref}^{24}\\
&- 1.480\cdot 10^{-45}\cdot\omega_{ref}^{25}\big)\cdot T_m
\end{aligned}
\tag{32}
$$

4.5. Discussion

After the SRM drive and control tests performed for an operating point in Case Study I, where speed and load torque provide mechanical power of approximately $P_m \approx 750$ W, other tests were performed for the range of operation with $50\ \text{rad/s} \le \omega_{ref} \le 150\ \text{rad/s}$ in Case Study III. Thus, the performance of drive and control types can be analyzed for different conditions (Case Study I, Case Study II and Case Study III), where the speed value varies from $50\ \text{rad/s} \le \omega_{ref} \le 150\ \text{rad/s}$ and the load applied to SRM shaft between $0.5\ \text{N m} \le T_L \le 5\ \text{N m}$.

In Case Study I and Case Study II, conventional drives with PID controller acting through excitation voltage (Case Study I) and through coil switching (Case Study II) were optimized with hybrid algorithm. For each case, the conditions are: (i) fixed speed $\omega_{ref} = 150$ rad/s and (ii) fixed load torque $T_L = 5$ N m. Since PID controller is a linear system with fixed gains, it is expected that the greater distance from the point of operation in which the control has been optimized, the lower its performance. Fig. 14(a) shows the performance of speed controller for three proposed drives, calculated by (18).

In this comparison, tests were run at $50\ \text{rad/s} \le \omega_{ref} \le 150\ \text{rad/s}$ and $0.5\ \text{N m} \le T_L \le 5\ \text{N m}$ for Case Study I, Case Study II and Case Study III and it was used the same range of ω_{ref} proposed to find the expressions (29) to (32). The SRM driving and control in Case Study III acts dynamically for the range of ω_{ref}. Under extrapolation conditions Case Study III acts as Case Study I, with fixed switching angles and controller gains.

Still in Fig. 14(a), it can be seen that Case Study III presented greater performance of superior speed for entire operation range. The control is optimized at approximately 185% when compared to Case Study I and 103% when compared to Case Study II. Considering same speed and same torque, the largest difference in Case Study III fitness function with respect to Case Study I was 520% and 268% in Case Study II. The control presents greater performance with lower value of fitness function, it is noted that the difference between values of fitness function using the model proposed in Case Study III, is greater in conditions than ω and T_L are furthest from the point of operation of $\omega = 150$ rad/s and $T_L = 5$ N m. The PID control system with dynamic gains has lower values of f_ω for entire range of operation.

Regarding the energy efficiency shown in Fig. 14(b), Case Study III is optimized at approximately 5.12% when compared to Case Study I and 44.36% when compared to Case Study II. Considering the same speed and the same torque, the largest difference in Case Study III fitness function values compared to Case Study I was 10.30% and 84.57% compared with Case Study II. It can be noticed that optimization percentage of energy efficiency, using the model proposed in Case Study III, is higher in low speed conditions, besides having larger values for the entire range of operation.

The DC current supplied to SRM via DC bus is shown in Fig. 14(c). The model proposed by Case Study III obtained lower current consumption than Case Study I. The torque ripple is shown in Fig. 14(d) where Case Study I produces smaller ripple at higher speeds.The SRM under study has high levels of torque ripple, especially in low speed operations. However, these oscillations can be minimized by altering some constructive features in the design of the machine, such as the number of poles, for example. Fig. 14(e) shows SRM electric power consumption, where in whole test range the Case Study III has lowest consumption in producing the same mechanical power as Case Study I and Case Study II.

The test with setpoint variation of speed controller and insertion of different values of mechanical load in SRM shaft was performed and can be visualized in Fig. 15. This test has simulation time of $t = 120$ s with values of $\omega_{ref} = [100, 50, 150, 120]$ rad/s in intervals of $t = 30$ s, and $T_L = [0, 5, 2, 3, 5, 1, 5, 5, 5, 5, 2, 5]$ N m at intervals of $t = 10$ s. Fig. 15(a) shows speed response of PID controller for Case Study I, Case Study II and Case Study III. It is observed the best performance in red color line, referring to Case Study III.

Fig. 15(b) shows energy efficiency values of SRM under the test conditions for Case Study I, Case Study II and Case Study III. Case Study III presents higher efficiency values in relation to other cases, especially when SRM operates at low speeds. Fig. 15(c) shows cumulative absolute error values over $t = 120$ s, where Case Study III obtained approximately 61.55% less cumulative error compared with Case Study I and 17.94% less compared with Case Study II.

The electric power consumption throughout t is presented in Fig. 15(d), where $P_e = 5552.93W$ for Case Study I, $P_e = 6442.36W$ for Case Study II and $P_e = 5421.61W$ for Case Study III. Case Study III has 2.42% lower power consumption than Case Study I and 18.82% compared with Case Study II, obtaining greater performance in speed control.

In the results presented, three tests were carried out for Case Study I, Case Study II and Case Study III. At the first case, a step signal was applied at speed reference $\omega_{ref} = 150$ rad/s with load torque of $T_L = 5$ N m. The results for the first test are given in Tables 4 and 5. In the second test step signals were applied at $50\ \text{rad/s} \le \omega_{ref} \le 150\ \text{rad/s}$ with load torque of $0.5N\cdot m \le T_L \le 5N\cdot m$. The results for the second test are given in Tables 6 and 7. In the third test, different values of ω_{ref} and T_L were applied, where $\omega_{ref} = [100, 50, 150, 120]$ rad/s, in intervals of $t = 30$ s, and $T_L = [0, 5, 2, 3, 5, 1, 5, 5, 5, 5, 2, 5]$ N m, in intervals of $t = 10$ s over $t = 120$ s. The results for the third test are given in Tables 8 and 9. In tests performed, Case Study I and Case Study II control systems were optimized at one operating point and for Case Study III the control system was optimized for the range $50\ \text{rad/s} \le \omega_{ref} \le 150\ \text{rad/s}$.

In Tables 4 and 5, Case Study III presented lower electrical power consumption P_e and consequently obtained greater energy efficiency η. Also in Tables 4 and 5, Case Study I obtained the lowest value of fitness function for the speed control. In Tables 6 and 7, Case Study I obtained the lowest average torque ripple $\overline{r_T}$, Case Study II obtained the lowest average excitation current consumption $\overline{I_{exc}}$ and Case Study III presented the best values of $\overline{P_e}$, $f_{\omega_{\max}}$, $f_{\omega_{\min}}$, $\overline{f_\omega}$, $\eta_{\max}$, $\eta_{\min}$ e $\overline{\eta}$. In Tables 8 and 9, Case Study III obtained the best values of $P_{e_{\max}}$, $P_{e_{\min}}$,

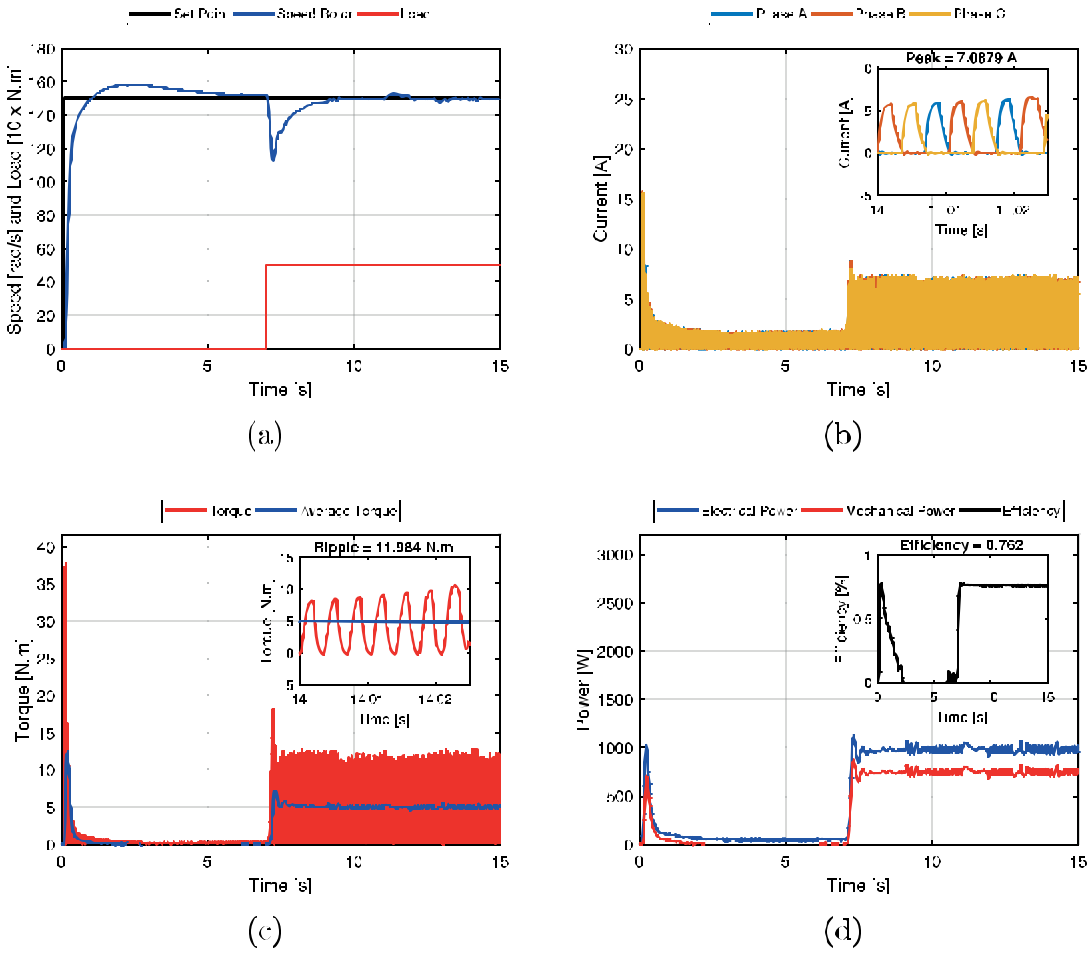

Fig. 13. PID controller acting on excitation voltage and setting dynamic switching angles: (a) speed response for ω_{ref} = 150 rad/s, (b) current per phase, (c) torque developed by the SRM and (d) input electrical power, mechanical output power and SRM energy efficiency.

Table 4
Tests performed for Case Study I, Case Study II and Case Study III with step applied at ω_{ref} = 150 rad/s and T_L = 5 N m.

Case study	θ_{on} [°]	θ_{off} [°]	k_p*	k_i*	k_d*
I	0	30	$2.29 \cdot 10^{-1}$	$2.98 \cdot 10^{-1}$	$7.98 \cdot 10^{-5}$
II	0	30	$8.08 \cdot 10^{-2}$	$8.78 \cdot 10^{-2}$	$7.77 \cdot 10^{-6}$
III	10.75	(29)	(30)	(31)	(32)

*Unit of measurement [° s/rad] for Case Study I and Case Study III; [A s/rad] for Case Study II.

Table 5
Tests performed for Case Study I, Case Study II and Case Study III with step applied at ω_{ref} = 150 rad/s and T_L = 5 N m.

Case study	P_e [W]	P_m [W]	f_ω [%]	η[%]
I	1004	756	**3.01**	0.753
II	1093	750	6.06	0.686
III	**988**	753	3.11	**0.762**

$\overline{P_e}$, IAE, $\eta_{\max}$, $\eta_{\min}$ and $\overline{\eta}$ when compared with Case Study I and Case Study II.

The results presented in this work provide comparative study between the driving and control methods for switched reluctance motor. In addition, it presents optimized method that ensures greater performance of SRM control and energy efficiency in wide operation range. The proposed method can be applied to switched reluctance machine

Table 6
Tests performed for Case Study I, Case Study II and Case Study III with step applied 50 rad/s $\leq \omega_{ref} \leq$ 150 rad/s and 0.5 N m $\leq T_L \leq$ 5 N m.

Case study	$\overline{T_T}$ [N m]	$\overline{I_{exc}}$ [A]	$\overline{P_e}$ [W]	$\overline{P_{mec}}$ [W]
I	**4.32**	2.97	396	274
II	5.88	**1.18**	623	274
III	5.97	1.58	**378**	274

Table 7
Tests performed for Case Study I, Case Study II and Case Study III with step applied 50 rad/s $\leq \omega_{ref} \leq$ 150 rad/s and 0.5 N m $\leq T_L \leq$ 5 N m.

Case study	$f_{\omega_{\max}}$ [%]	$f_{\omega_{\min}}$ [%]	$\overline{f_\omega}$ [%]	$\eta_{\max}$ [%]	$\eta_{\min}$ [%]	$\overline{\eta}$ [%]
I	11.96	1.38	6.09	75.45	48.62	66.03
II	7.90	2.26	4.32	64.97	8.35	39.65
III	**3.82**	**1.24**	**2.24**	**76.85**	**51.68**	**69.55**

Table 8
Tests performed for Case Study I, Case Study II and Case Study III with ω_{ref} = [100, 50, 150, 120] rad/s at intervals of t = 30s and different T_L which t = 10 s.

Case study	$P_{e_{\max}}$ [W]	$P_{e_{\min}}$ [W]	$\overline{P_e}$ [W]	$P_{m_{\max}}$ [W]	$P_{m_{\min}}$ [W]	$\overline{P_m}$ [W]
I	999	94.48	555	754	51	389
II	1093	145.42	644	750	51	389
III	**988**	**85.37**	**542**	753	51	392

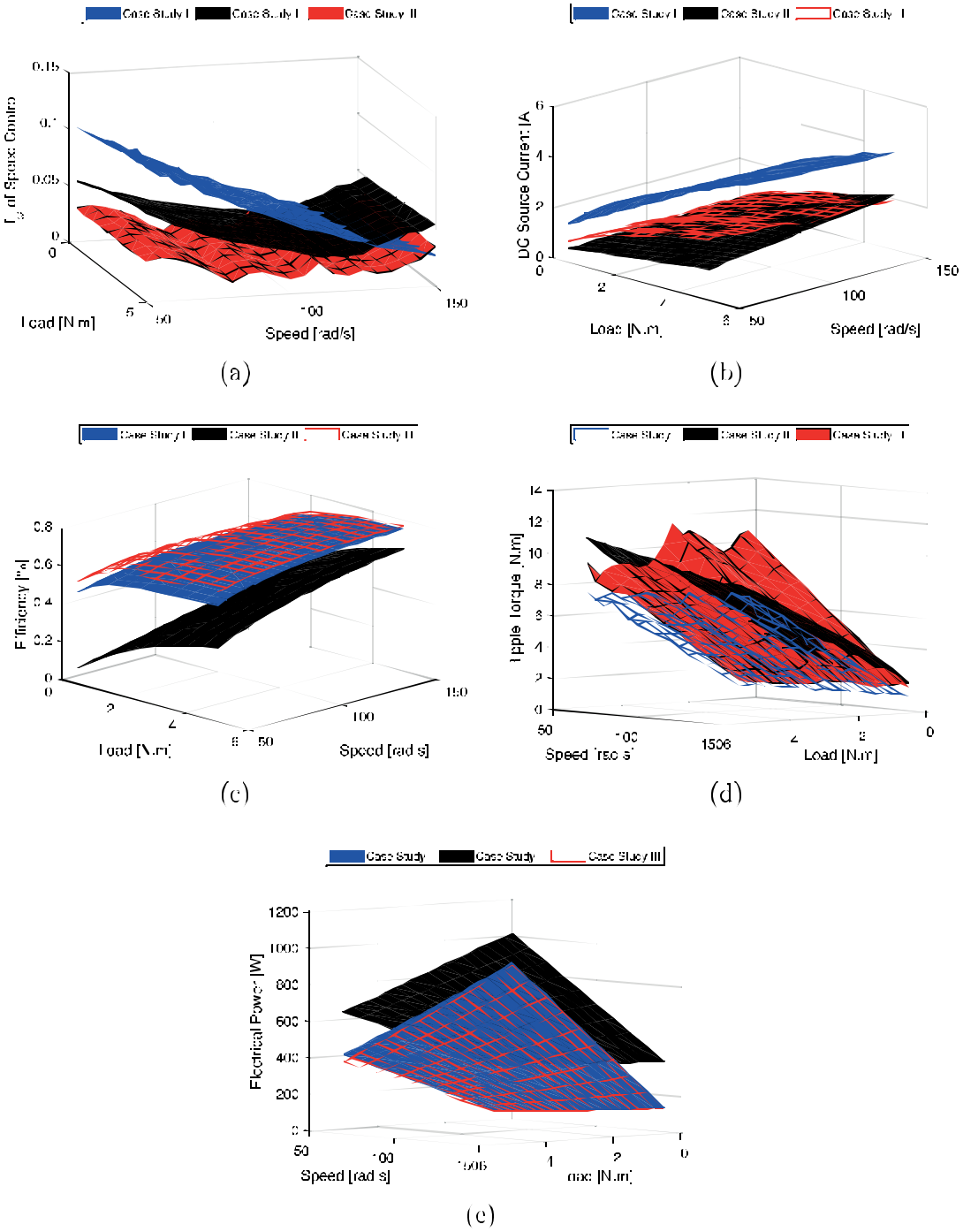

Fig. 14. Tests performed for Case Study I, Case Study II and Case Study III with load steps applied at 50 rad/s $\leq \omega_{ref} \leq$ 150 rad/s and 0.5 N m $\leq T_L \leq$ 5 N m: (a) fitness function related to the PID controller, (b) efficiency, (c) DC bus current, (d) SRM torque ripple and (e) power consumed by SRM.

Table 9
Tests performed for Case Study I, Case Study II and Case Study III with ω_{ref} = [100, 50, 150, 120] rad/s at intervals of t = 30 s and differents T_L which t = 10 s.

Case study	IAE[rad]	η_{max}[%]	η_{min}[%]	$\overline{\eta}$[%]
I	349	75.14	54.5	69.18
II	296	65.07	35.24	58.56
III	**216**	**76.32**	**60.51**	**72.14**

under conditions of electric power generation, allowing the optimized operation with reversibility of energy conversion dynamically. For development of Case Study III methodology, the relationship between coil switching angles and energy efficiency was analyzed, which made it difficult to operate the speed control. Thus, the technique of dynamic adjustment of controller gains was developed. For reproduction of this methodology, one must obtain optimized PID controller gains before performing any other test about behavior of switching angles, since the switching angles change considerably the system behavior (Saraiva

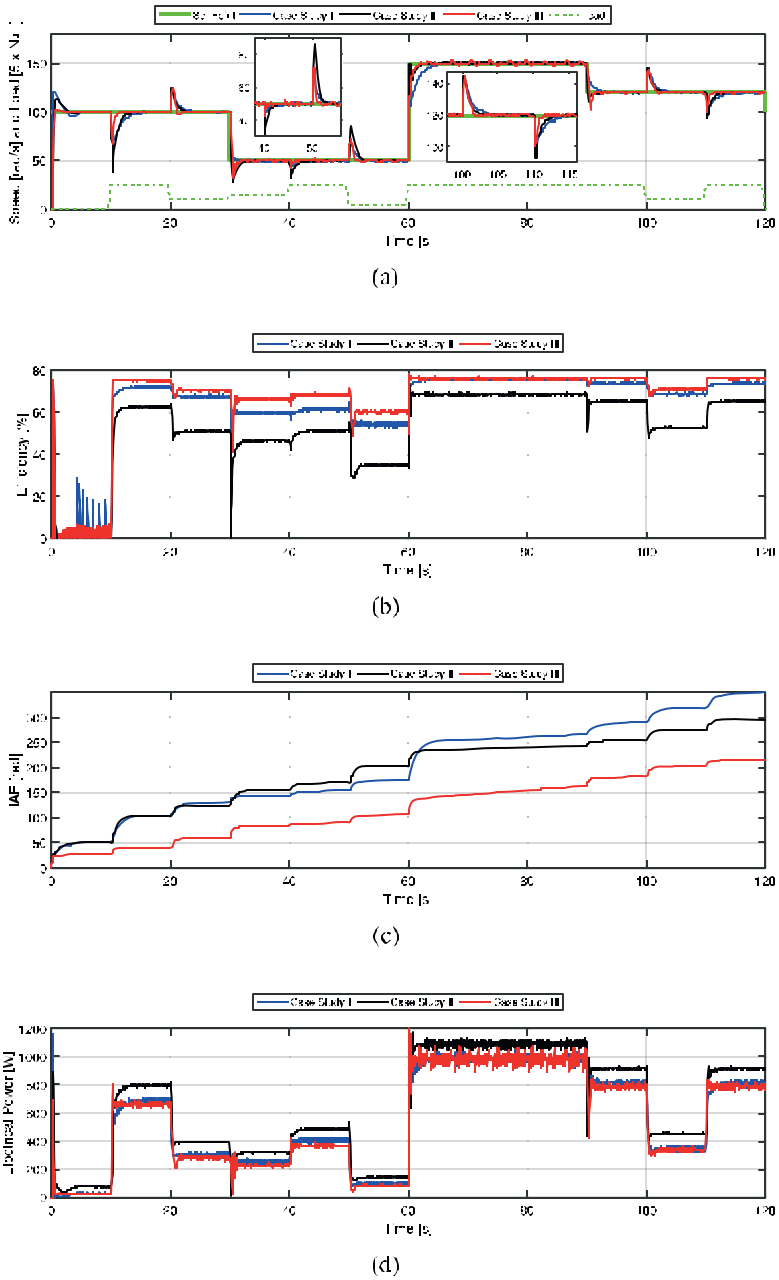

Fig. 15. Test with variation of ω_{ref} and T_L: (a) SRM speed and load torque, (b) efficiency, (c) accumulated absolute error and (d) power consumed by SRM.

et al., 2017). Thus, higher precision of collected data is obtained in a shorter simulation time, considering that optimized PID controller has a shorter response time ensure null error in steady state.

In order to compare the results obtained in the Case Study III with other methods used in automatic control, a comparative study was carried out between the Case Study III and the work of Wang, Tseng, and Chien (2011). The study by Wang et al. (2011) employs an $8x6$ topology SRM used for the development of adaptive fuzzy speed control. Table 10 presents a comparison of some SRM parameters of this work, taken from Table 2, and SRM parameters taken from Wang et al. (2011). Also in Table 10 is presented a comparative of some control performance parameters performed in Case Study III and control performance parameters performed in the work of Wang et al. (2011).

Table 10
Comparison between Case Study III and work by Wang et al. (2011).

Parameters	Case study III	Wang et al. (2011)
Settling time [s]	≈ 7.00	≈ 1.00
Rising time [s]	≈ 1.00	≈ 1.00
Overshoot [%]	≈ 5.10	≈ 2.60
Inertia [(N m s^2)/rad	$1.60 \cdot 10^{-2}$	$1.70 \cdot 10^{-3}$
Viscous friction [(N m s)/rad]	$1.65 \cdot 10^{-2}$	$1.00 \cdot 10^{-3}$
Phase resistance [Ω]	3.11	0.13
Aligned inductance [mH]	255	3.60
Unaligned inductance [mH]	32	0.43

It can be observed that the performance parameters related to the work of Wang et al. (2011) such as settling time, rising time and

overshoot, have better values when compared to Case Study III. However, the SRM of Wang et al. (2011) has different electromechanical parameters of the SRM using in this work, which makes the SRM of Wang et al. (2011) has minor transient response. The adaptive fuzzy controller used by Wang et al. (2011) is compared with the classical PI controller and the adaptive fuzzy controller has better results in tests with perturbations. The adaptive fuzzy controller can be used in the model presented in this work. However, it will be necessary a greater computational effort.

5. Conclusions

In this work were presented techniques of modeling, driving and classic speed control for switched reluctance motor. The proposed identification method by parametric regression turn it possible to find an model that represents SRM nonlinear inductance profile in an optimized way, considering the magnetic saturation. Some representing methods of nonlinear inductance profile present in literature were discussed. It was consider the parametric regression model has higher precision, besides requiring less computational effort, when compared to nonlinear models available in the literature. From the proposed model, conventional drive and control techniques for SRM were discussed in which excitation voltage or switching angles were fixed, and drives in which excitation voltage and switching angles were dynamic. The aim was to obtain a better response of speed control and energy efficiency. The PID controller was used because they has low computational cost, simplified implementation and maintenance compared to modern controllers. However, system identification methods were used in order to find expression that represents dynamic behavior of controller gains in a wide speed range, where gains provided optimized speed control. System identification method was also used to find expression that represented dynamic behavior of SRM switching angles, so for a given speed control range, better energy efficiency was obtained. At specific case, in which drive and control have a dynamic behavior, it is possible to obtain: (i) low computational cost, simplified implementation and maintenance, because it is the classical PID controller dynamically, (ii) greater control performance, when compared to PID controller with fixed gains and (iii) higher energy efficiency when compared to drives where excitation voltage or switching angles are fixed. The techniques presented in this work ensure improvement in drive and control of switched reluctance motor, being able to be applied optimally, under conditions of speed variations, torque variations and cost reductions: (i) implementation, (ii) maintenance and (iii) energy consumption.

Acknowledgments

The authors would like to thank National Council for Scientific and Technological Development (CNPq), Foundation for Research Support of the State of Goias (FAPEG) and Brazilian Federal Agency for Support and Evaluation of Graduate Education (CAPES) for scholarships: 88881.133454/2016-01 and 88881.132192/2016-01.

Declaration of competing interest

None declared.

References

Andrade, D. A., & Krishnan, R. (2001). Characterization of switched reluctance machines using series approach. In *IEEE conference publications*.

Araujo, W. R. H. (2006). Design and construction of a prototype and implementation of switching strategies of a switched reluctance motor (thesis in portuguese), Federal University of Goias.

Araujo, W. R. H., Reis, M. R. C., Calixto, W. P., Wainer, G. A., Magalhaes, A. S., & Gomes, F. A. (2017). Nonlinear simulation methodology for switched reluctance machine using induction profile found by parametric regression. In *IEEE conference publications*.

Fitzgerald, A. E., Kingsley, C., & Umans, S. D. (2013). *Electric machinery* (p. 1). McGraw-Hill Science.

Fujishiro, S., Ishikawa, K., Kikuchi, S., Nakamura, K., & Ichinokura, O. (2006). Design of outer-rotor-type multipolar switched reluctance motor for electric vehicle. *Journal of Applied Physics*, 08R324.

Gobbi, R., Rajendran, S., Ramar, K., Ahamed, M. K., & Anayet, K. (2008). Study on inductance measurement techniques for switched reluctance motors. In *Proceedings of EnCon2008*.

Gomes, F. A., Assis, A. O., Reis, M. R. C., Gomes, V. M., Oliveira, S. G. M., Araujo, W. R. H., & Calixto, W. P. (2017). Proposal of heuristic regression method applied in descriptive data analysis: case studies. *Transactions on Environment and Electrical Engineering*.

Hannoun, H., Hilairet, M., & Marchand, C. (2011). High performance current control of a switched reluctance machine based on a gain-scheduling PI controller. *Control Engineering Practice*, 1377–1386.

Kazmierkowski, M. P., Blaabjerg, F., & Krishnan, R. (2002). *Control in power electronics* (p. 1). Academic Press.

Kosow, I. L. (1991). *Electric machinery and transformers* (p. 1). Pearson College Div.

Law, A. M., & Kelton, W. D. (2000). *Simulation modeling and analysis* (p. 1). MA: McGraw Hill Boston.

N. d.S., Nise (2010). *Control systems engineering* (p. 1). LTC.

Ogata, K. (2009). *Modern control engineering* (p. 1). Pearson.

Rashid, M. H. (2014). *Power electronics: circuits, devices, and applications* (p. 1). Pearson.

Reis, M. R. C., Alvarenga, B., Silva, W. G., Ganzaroli, C. A., Calixto, W. P., Araujo, W. R. H., Alves, A. J., & Domingues, E. G. (2013). Heuristic and deterministic strategies applied on a pid controller tuning for speed control of a dc motor. In *IEEE conference publications*.

Reis, M. R. C., Araujo, W. R. H., & Calixto, W. P. (2017). Efficiency improvement of switched reluctance generator using optimization techniques. *Transactions on Environment and Electrical Engineering*.

Reis, M. R. C., Araujo, W. R. H., Calixto, W. P., & Alves, A. J. (2015). Analysis of switched reluctance motor efficiency under different speed control strategies. In *IEEE conference publications*.

Saraiva, J. P., Lima, B. S., Gomes, V. M., Flores, P. H. R., Gomes, F. A., Assis, A. O., Reis, M. R. C., Araujo, W. R. G., Abrenhosa, C., & Calixto, W. P. (2017). Calculation of sensitivity index using one-at-a-time measures based on graphical analysis. In *18th international scientific conference on eletric power engineering (EPE)*.

Shaoping, S., & Qingfu, L. (2001). Design of multi-pole single phase switched reluctance generator. In *Electrical machines and systems, 2001. ICEMS 2001. Proceedings of the fifth international conference on: Vol. 2* (pp. 938–941).

Silveira, A. W. F. V., Andrade, D. A., Fleury, A., Gomes, L. C., Bissochi, C. A., & Dias, R. J. (2009). Voltage control in starter/generator SRM based systems. In *2009 IEEE energy conversion congress and exposition* (pp. 2460–2465).

Soderstrom, T., & Stoica, P. (1989). *System identification* (p. 1). Prentice Hall.

Su, Z., Zhang, C., Wang, M., & Dai, Z. (2017). Research on switched reluctance motor speed control system based on robust control. In *IEEE conference publications*.

Viajante, G. P., Andrade, D. A., Gomes, L. C., Freitas, M. A. L., Bernadeli, V. R., & Silveira, A. W. F. V. (2013). A voltage control strategy for switched reluctance generator. In *IEEE international electric machines and drives conference - IEMDC*.

Wang, S. Y., Tseng, C. L., & Chien, S. C. (2011). Adaptive fuzzy cerebellar model articulation control for switched reluctance motor drive. In *IET electric power applications*. IEEE.

Watanabe, K., Aida, S., Komatsuzaki, A., & Miki, I. (2008). Basic characteristics of electric vehicle using 40kw switched reluctance motor. In *2008 international conference on electrical machines and systems* (pp. 3358–3361).

Zhang, P., Cassani, P. A., & Williamson, S. S. (2010). An accurate inductance profile measurement technique for switched reluctance machines. *IEEE Transactions on Industrial Electronics*.

Zheng, J., Zhao, S., & Wei, S. (2009). Application of self-tuning fuzzy PID controller for a SRM direct drive volume control hydraulic press. *Control Engineering Practice*, 1398–1404.